

AD-A270 127



2

PL-TR-93-2124

**ASPECTS OF THE CALIBRATION AND PROCESSING OF THE CRRES FLUXGATE MAGNETOMETER DATA**

W. J. McNeil

**S DTIC ELECTE D**  
**A SEP 14 1993**

Radex, Inc.  
Three Preston Court  
Bedford, MA 01730

May 21, 1993

Original contains color plates; All DTIC reproductions will be in black and white.

Scientific Report No. 1

Approved for public release; distribution unlimited

**93-21393**

62p43



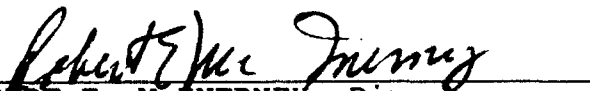
**PHILLIPS LABORATORY**  
**Directorate of Geophysics**  
**AIR FORCE MATERIEL COMMAND**  
**HANSCOM AIR FORCE BASE, MA 01731-3010**

93 0 1 067

"This technical report has been reviewed and is approved for publication"



EDWARD C. ROBINSON  
Contract Manager  
Data Analysis Division



ROBERT E. MCINERNEY, Director  
Data Analysis Division

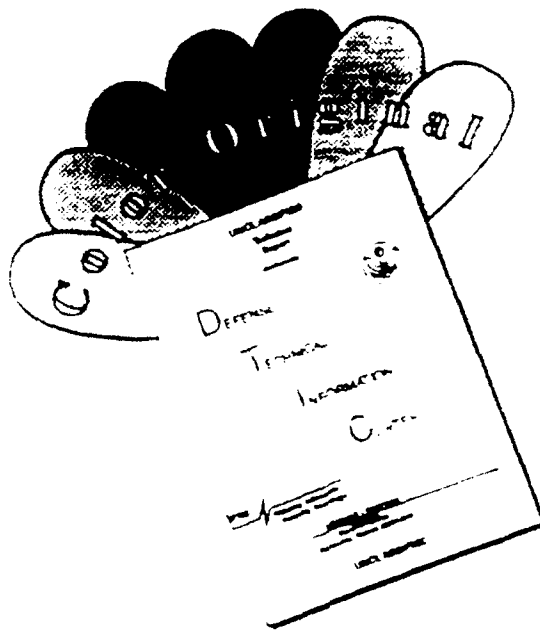
This report has been reviewed by the ESD Public Affairs Office (PA) and is releasable to the National Technical Information Service (NTIS).

Qualified requestors may obtain additional copies from the Defense Technical Information Center. All others should apply to the National Technical Information Service.

If your address has changed, or if you wish to be removed from the mailing list, or if the addressee is no longer employed by your organization, please notify PL/TSI, 29 Randolph Road, Hanscom AFB, MA 01731-3010. This will assist us in maintaining a current mailing list.

Do not return copies of this report unless contractual obligations or notices on a specific document requires that it be returned.

# DISCLAIMER NOTICE



THIS DOCUMENT IS BEST QUALITY AVAILABLE. THE COPY FURNISHED TO DTIC CONTAINED A SIGNIFICANT NUMBER OF COLOR PAGES WHICH DO NOT REPRODUCE LEGIBLY ON BLACK AND WHITE MICROFICHE.

# REPORT DOCUMENTATION PAGE

Form Approved  
OMB No. 0704-0188

Public reporting burden for this collection of information is estimated to average 1 hour per response, including the time for reviewing instructions, searching existing data sources, gathering and maintaining the data needed, and completing and reviewing the collection of information. Send comments regarding this burden estimate or any other aspect of this collection of information, including suggestions for reducing this burden, to Washington Headquarters Services, Directorate for Information Operations and Reports, 1215 Jefferson Davis Highway, Suite 1204, Arlington, VA 22202-4302, and to the Office of Management and Budget, Paperwork Reduction Project (0704-0188), Washington, DC 20503

1. AGENCY USE ONLY (Leave blank)	2. REPORT DATE 21 May 1993	3. REPORT TYPE AND DATES COVERED Scientific Report No. 1	
4. TITLE AND SUBTITLE  Aspects of the Calibration and Processing of the CRRES Fluxgate Magnetometer Data		5. FUNDING NUMBERS  PE 62101F PR 7659 TA GY WU AA  Contract F19628-93-C-0023	
6. AUTHOR(S)  W. J. McNeil		8. PERFORMING ORGANIZATION REPORT NUMBER  RXR-930501	
7. PERFORMING ORGANIZATION NAME(S) AND ADDRESS(ES)  RADEX, Inc. Three Preston Court Bedford, MA 01730		10. SPONSORING / MONITORING AGENCY REPORT NUMBER  PL-TR-93-2124	
9. SPONSORING / MONITORING AGENCY NAME(S) AND ADDRESS(ES)  Phillips Laboratory 29 Randolph Road Hanscom AFB, MA 01731-3010  Contract Manager: Edward C. Robinson/GPD		11. SUPPLEMENTARY NOTES	
12a. DISTRIBUTION / AVAILABILITY STATEMENT Approved for Public Release Distribution Unlimited		12b. DISTRIBUTION CODE	
13. ABSTRACT (Maximum 200 words)  The report describes algorithms for on-orbit calibration and processing of the Fluxgate Magnetometer data from the Combined Release and Radiation Effects Satellite. The calibration problem is parameterized in a completely general treatment in terms of instrument alignment and magnetometer offsets and gains. Fits to the data from the spinning satellite are used to derive all but two of the parameters needed for despinning. Data taken during precession maneuvers and attitude data is used to derive these remaining two. The report includes a discussion of anomalies in the instrument and includes a description of the data products.			
14. SUBJECT TERMS  Magnetometer calibration, Magnetometer analysis, CRRES magnetometer		15. NUMBER OF PAGES 62	
17. SECURITY CLASSIFICATION OF REPORT Unclassified		16. PRICE CODE	
18. SECURITY CLASSIFICATION OF THIS PAGE Unclassified		19. SECURITY CLASSIFICATION OF ABSTRACT Unclassified	
20. LIMITATION OF ABSTRACT  Unlimited			

## Table of Contents

Section	Page
1. INTRODUCTION	1
2. THE SATELLITE AND INSTRUMENT	2
3. PRE-LAUNCH ACTIVITIES	3
4. CALIBRATION	4
4.1. The Attitude	5
4.2. Reduction to One-Second Data	7
4.3. The Spin Fit	9
4.4. The Calculation of Alignments	11
4.5. The Calculation of Gain Ratios	21
4.6. The Calculation of Offsets	25
4.7. The Calculation of Gains	26
5. CALCULATION OF THE ASSUMED QUANTITIES	26
5.1. The Calculation of $\Delta_3$	29
5.2. The Calculation of the X-Sensor Phase	35
5.3. The Calculation of Absolute Gain	36
6. DESPINNING AND DATA PRODUCTS	37
6.1. The Two-Second Data Base	40
6.2. The VDH Survey Plot	43
6.3. The Ultra-Low Frequency Spectrogram	43
6.4. The Ion Cyclotron Spectrogram	43
6.5. 16-Sample/second Processing	43
6.6. Quick Look Plots	47
7. CONCLUSION	47
REFERENCES	48
APPENDIX	49

## List of Figures

Figure	Page
1. Sample attitude quality control/survey plot . . . . .	6
2. Sample sensor signals from low field . . . . .	10
3. Calculated relative sensor phase $\phi_{ij}$ . . . . .	13
4. Calculated gain modified elevation cosine ratio $\gamma_{ij}$ . . . . .	14
5. Calculated gain modified elevation sine ratio $\delta_{ij}$ . . . . .	15
6. Alignments calculated for Orbits 410-450 . . . . .	20
7. Calculated low gain ratio of y-sensor to x-sensor gains . . . . .	22
8. Calculated high gain ratio of x-sensor to z-sensor gains . . . . .	23
9. Calculated ratio between low to high gain in the x-sensor . . . . .	24
10. Calculated value of the spin-plane offset $\Delta_1$ in high gain . . . . .	27
11. Calculated 5-minute averaged sensor offsets in high gain . . . . .	28
12. Magnetic field in the spacecraft frame . . . . .	30
13. The beginning of nutation following an attitude adjustment . . . . .	32
14. Magnetic field magnitude minus model as a function of $D_z$ . . . . .	33
15. A series of $D_z$ calculations following an attitude adjust . . . . .	34
16. Quality control plot to examine spin tone in spacecraft coordinate fields . . . . .	38
17. Quality control plot of spin tone in high gain . . . . .	39
18. Quality control plot of model field angle and magnitude deviation from measured field . . . . .	41
19. Quality control plot of measured minus model field . . . . .	42
20. VDH survey plot . . . . .	44
21. Ultra-low frequency spectrogram . . . . .	45
22. Ion cyclotron wave spectrogram . . . . .	46

## List of Tables

Table	Page
1. The Observables and the Assumed Quantities . . . . .	5
2. Sensor Orthogonality . . . . .	16

Accession For	
NTIS CRA&I	<input checked="" type="checkbox"/>
DTIC TAB	<input type="checkbox"/>
Unannounced	<input type="checkbox"/>
Justification	
By	
Distribution/	
Availability Codes	
Dist	Avail and/or Special
A-1	

**DTIC QUALITY INSPECTED 1**

## Acknowledgments

We are indebted to Howard J. Singer, who was primarily responsible for the success of this experiment and whose careful forethought produced a processing system ready for almost any aberrant behavior of the instrument. Working with him over the past few years has been a tremendously rewarding experience professionally, as well as a distinct pleasure. We also thank RMS Technologies, Inc., who directed telemetry acquisition and processing and who were extremely cordial in several times interrupting their own mission to provide rapid access to recent data during periods of mysterious behavior. Most of the batch processing was performed by Rich Ludlow, who also supplied several helpful suggestions for improving the operation of the system.

## 1. Introduction

The Fluxgate Magnetometer Experiment (AFGL 701-13-1) aboard the Combined Release and Radiation Effects Satellite (CRRES, P86-1) was designed to provide several important measurements [Singer, *et al.*, 1991]; (1) to provide magnetic field pitch angles for analysis of the particle instrument data; (2) as a diagnostic of global and local geomagnetic disturbances; (3) as a diagnostic of low frequency waves in the ambient environment; (4) to provide plasma gyrofrequencies; (5) to measure  $v \times B$  electric fields; (6) to support the chemical release activities and (7) to provide a secondary source of attitude information.

The calibration and processing system used on the data was the result of several years of analysis, simulation and software development. The system performed extremely well, allowing the calibration factors for the instrument to be available virtually from the start of the mission, in spite of a misdeployment of the instrument that led to pointing directions of the axes that were different from those planned by over  $18^\circ$ . The processing also resulted in a data set that was, for the most part, extremely clear of contamination from spacecraft induced fields and from 'spin tone' which is often a problem in magnetometer data from a spinning spacecraft. The processing proved to be relatively trouble free, most of it ultimately performed in batch, with little human intervention necessary.

Although the CRRES mission is now finished, it still seems worthwhile to set down a reasonably detailed account of what was done in the course of processing. This may prove valuable in thinking about processing for future missions. However, it is also valuable simply because the CRRES data itself is valuable and will, no doubt, be examined for years to come. Although a preliminary description of the processing system has been published [McNeil, 1987], we feel that the present retrospective, which includes many additional features resulting from experience with real data, will provide a more comprehensive summary.

Since routine processing of the data is finished, this document will not dwell on file formats and features important in the operation of the processing system itself. These can be inferred adequately from the software. Instead, we will aim for more of a descriptive account of how the data got to be what it is. We attempt to include all aspects that proved to be important in the processing, which we enumerate as follows: (1) the assessment of the attitude, (2) the reduction of the high frequency data to an edited, manageable data set, (3) the calculation of the instrument's alignment, (4) the calculation of gain ratios and offsets, (5) the calculation of absolute gain, (5) the process of quality control of the calibration, and (6) the survey plots and product data bases generated in the processing. These are discussed in the following sections, after a brief description of the satellite and the instrument. In addition, we will attempt to include details that may be important for reference when using the data products, such as specifics of the editing and averaging process used to create the product data bases and details on the generation of the summary plots and spectrograms. For reference, and because they are not documented elsewhere in a convenient format, the most complicated file formats and contents are included as an appendix.

## 2. The Satellite and Instrument

The satellite was launched in July of 1991, with a period of 9 hours 52 minutes, an inclination of  $18.2^\circ$ , a 350 km perigee and initial apogee of about 35,000 km altitude. CRRES was a spin-stabilized satellite with a spin rate of around 2 rpm. During a single orbit, the satellite encountered magnetic fields from as high as 35,000 nT down to less than 100 nT, meaning that the magnetometer instrument required a large dynamic range. Moreover, the rapid traversal of perigee, at speeds of over 11 km/sec, gave the changes in field magnitude and direction important for successful calibration. The satellite required the sun to spin axis angle to be greater than  $5^\circ$ , for adequate attitude calculation, and less than  $15^\circ$ , for adequate operation of the solar panels. This attitude requirement was satisfied by periodic precession maneuvers. These maneuvers were both a problem and a boon for calibration. Although routine calibration on an orbit with an attitude maneuver proved impossible, the motion of the satellite immediately after the adjustment allowed for the calculation of the spin axis offset, one of the parameters not immediately available from the on-orbit calibration scheme. The attitude adjustments also caused a moderately severe and long term oscillation of the satellite through interaction with the 50 meter wire booms. This showed up in magnetometer data for a few orbits after adjustments had taken place as a 20-minute sine wave, but did not interfere significantly with calibration.

The tri-axial fluxgate magnetometer was built by Schonstedt Instruments Co. It was mounted on a rigid Astromast boom, 6.1 meters long and about 7.5 meters from the center of the satellite. The magnetometer was linked to the Langmuir Probe/Electric Field experiment for power, signal processing and telemetry formatting. Each axial component of the measured magnetic field was reported approximately 16 times per second with a dynamic range of either 45,000 nT in low gain or 800 nT in high gain. With 12 bit quantization, this gave a resolution of about 22 nT and 0.4 nT in low and high gain respectively. On-board, the analog sensor signals were filtered successively by 60-Hz and 6-Hz low pass filters to remove aliasing. The telemetry multiplexer then sampled and separated each sensor into a low gain unamplified and a high gain signal amplified by about 50. If the amplified signal would not saturate the A/D converter, it was entered into telemetry. Otherwise, the low gain signal was sent. The three axis signals were simultaneous to about 150  $\mu$ s. In addition to the variable gain data, a low gain sample from the three sensors was sent about each half-second. The actual timing is 64 variable gain samples per master frame, which was nominally 4.096 seconds. Frequently in the following, the terms one-second or two-second will be used to indicate the frame rate divided by four and two respectively.

Originally, the magnetometer x-axis was to be directly along the negative x-axis of the satellite. The y-axis was to be nearly along the negative z-axis (spin axis) and the z-axis along the negative y-axis of the satellite, but with the whole assembly rotated about  $2.5^\circ$  around the x-axis. This was to allow for spin tone in the y-sensor measurement for on-orbit calibration purposes. After deployment, inspection of the data indicated that the boom had not fully extended. This led to an elevation of the x-axis of the magnetometer that was initially more than  $18^\circ$  above the spin plane. This angle changed slowly in time, from orbit to orbit, indicating that

the boom may have been restricted by a cable in the last few degrees of its final turn. The boom never did fully deploy, reaching only about 13° at the end of the mission. Fortunately, the calibration algorithms allowed for a fully general alignment of the instrument and for the direct calculation of arbitrary alignments, so that the data quality did not suffer.

### 3. Pre-Launch Activities

Prior to launch of the satellite, which was delayed several years by the hiatus in the Space Transport System program and which was eventually completed by the substitution of an Atlas rocket, a great deal of effort was expended in the simulation of the magnetometer data and development of algorithms and software for analysis. A description of the simulation and of preliminary analysis algorithms has already been recorded [McNeil and Singer, 1986]. However, it bears comment that this simulation program was considerably extended by launch to incorporate many features that served to improve the realism as well as to provide for detailed testing of the analysis and processing software.

Satellite attitude data for the simulation and analysis was obtained from Attitude Fit Coefficients generated by the CRRES Attitude Determination Program (CADP) from realistic simulated orbits and raw attitude data developed in another program [McNeil and McInerney, 1988]. Simulation and analysis was carried out using the same ephemeris data files that would be used in actual operation of the system. This meant, too, that the structure was already present to easily simulate signals for comparison with real data. This operation was in fact carried out several times initially and aided greatly in the efficient trouble shooting of some minor problems.

Additionally, simulations in cooperation with the development of the overall Orbital Data Processing System testing program, incorporated realistic magnetometer data into simulated raw telemetry files and attempted to recover these data from both the magnetometer experiment file and from the more generally available magnetic field file. The combination of these simulations allowed realistic and verifiable data to flow from start to end of the processing. As a result, there was minimal difficulty in performing a full analysis on the first available data set. Although this sort of simulation program might well have been excessively ambitious, had we been charged only with the magnetometer software instead of the attitude, ephemeris and orbital data processing tasks as well, it was certainly beneficial to the software development process.

In addition to the simulation of nominal behavior, several studies were carried out to examine the effects of errors in required input values, of spacecraft wobble and of nutation. Experience with these simulated anomalies allowed for increased familiarity with the satellite and instrument behavior as well as providing confidence levels of the calibration results. Finally, just prior to launch, optical alignment data taken by Ball Aerospace, orthogonality data provided by Schonstedt, and the many meticulous ground measurements made by the experimenter were analyzed to provide a set of initial estimates to the required quantities.

## 4. Calibration

The calibration efforts were designed for two distinct purposes; (1) the generation of calibration factors for the use of other experimenters in the calculation of pitch angle and of the magnetic field and (2) the creation of a calibrated, inertial data set for the use of the magnetometer experimenter. This treatment was somewhat unique in that calibration *factors* were provided, along with the instrument readings in counts, rather than a file of calibrated geophysical measurements. In this way, calibration of the instrument could lag the overall satellite data processing slightly without causing a disruption in the data processing flow. Since the CRRES mission involved tens of experiments with data going out to locations world-wide, this arrangement was especially practical. A subroutine was provided to experimenters which read the magnetic field file and the calibration data file, giving calibrated sensor readings in either sensor or spacecraft coordinates. The distinction between the two products, the calibration factors and the calibrated data, is important. For the calibration factors disseminated to the community, it was deemed adequate to provide one set per orbit, averaging over the small perturbations in offsets arising from spacecraft induced fields, while for the final inertial data set, these perturbations were generally removed by calculating offsets on a shorter time scale.

Providing calibration factors orbit by orbit turned out to be especially important since the alignment of the instrument changed by almost 5° over the course of the mission. Providing raw data with updatable calibrations was also convenient in that the incorporation of the approximately 2.5° phase shift, uncompensated for in the calibration of most orbits before Orbit 700, could be easily made, resulting in dramatically improved accuracy of the spacecraft frame magnetic field.

We think of calibration as the calculation of the position of each of the three axes in spacecraft coordinates, the three axis offsets  $d_i$  and the gains  $g_i$ , all of which are necessary to transform the measured sensor signal into the magnetic field in spacecraft coordinates. The sensor readings are related to the external magnetic field by the equation

$$\begin{bmatrix} s_x \\ s_y \\ s_z \end{bmatrix} = \begin{bmatrix} g_x^{-1} & 0 & 0 \\ 0 & g_y^{-1} & 0 \\ 0 & 0 & g_z^{-1} \end{bmatrix} \begin{bmatrix} \cos\theta_x \cos\phi_x & \cos\theta_x \sin\phi_x & \sin\theta_x \\ \cos\theta_y \cos\phi_y & \cos\theta_y \sin\phi_y & \sin\theta_y \\ \cos\theta_z \cos\phi_z & \cos\theta_z \sin\phi_z & \sin\theta_z \end{bmatrix} \begin{bmatrix} b_x \\ b_y \\ b_z \end{bmatrix} + \begin{bmatrix} d_x \\ d_y \\ d_z \end{bmatrix} \quad (1)$$

where  $\theta_i$  is the elevation and  $\phi_i$  the phase of each of the magnetometer axes in the spacecraft coordinate system.  $b_i$  are the components of the external field in the spacecraft frame. The gains,  $g_i$ , have been inverted in Eq(1) so that they have units of nT/count. The offsets,  $d_i$ , have units of counts as do the  $s_i$ 's. We perform calibration in stages, first calculating the elevations  $\theta_i$  and relative phases  $\phi_{xi} \equiv \phi_i - \phi_x$ . Next, we find the *ratios* of the gains and the offsets. Following this, we find the absolute gain. These are performed on an orbit-by-orbit bases. Two other quantities, the offset along the spin axis and the absolute phase of the x-sensor, are obtained less frequently by other means.

Our approach to on-orbit calibration is to separate the magnetometer signals from the three sensor axes into spin modulated and constant components. By the manipulation of these values and the ratios between the sensors, we are able to determine eight independent quantities altogether. Eq(1) shows, however, that there are four more quantities left to be determined to fully specify the alignments, gains and offsets. For routine orbit-by-orbit calibration, these quantities are assumed to be known from the outset. In the course of processing, however, each of these was independently calculated by other methods, either as values to substitute into the orbit-by-orbit processing or simply to verify that the pre-flight estimates were of sufficient accuracy. Table 1 below gives a description of the required quantities, the quantities available from on-orbit measurements and the assumed quantities required to complete the calculation of each set.

Table 1. The Observables and the Assumed Quantities

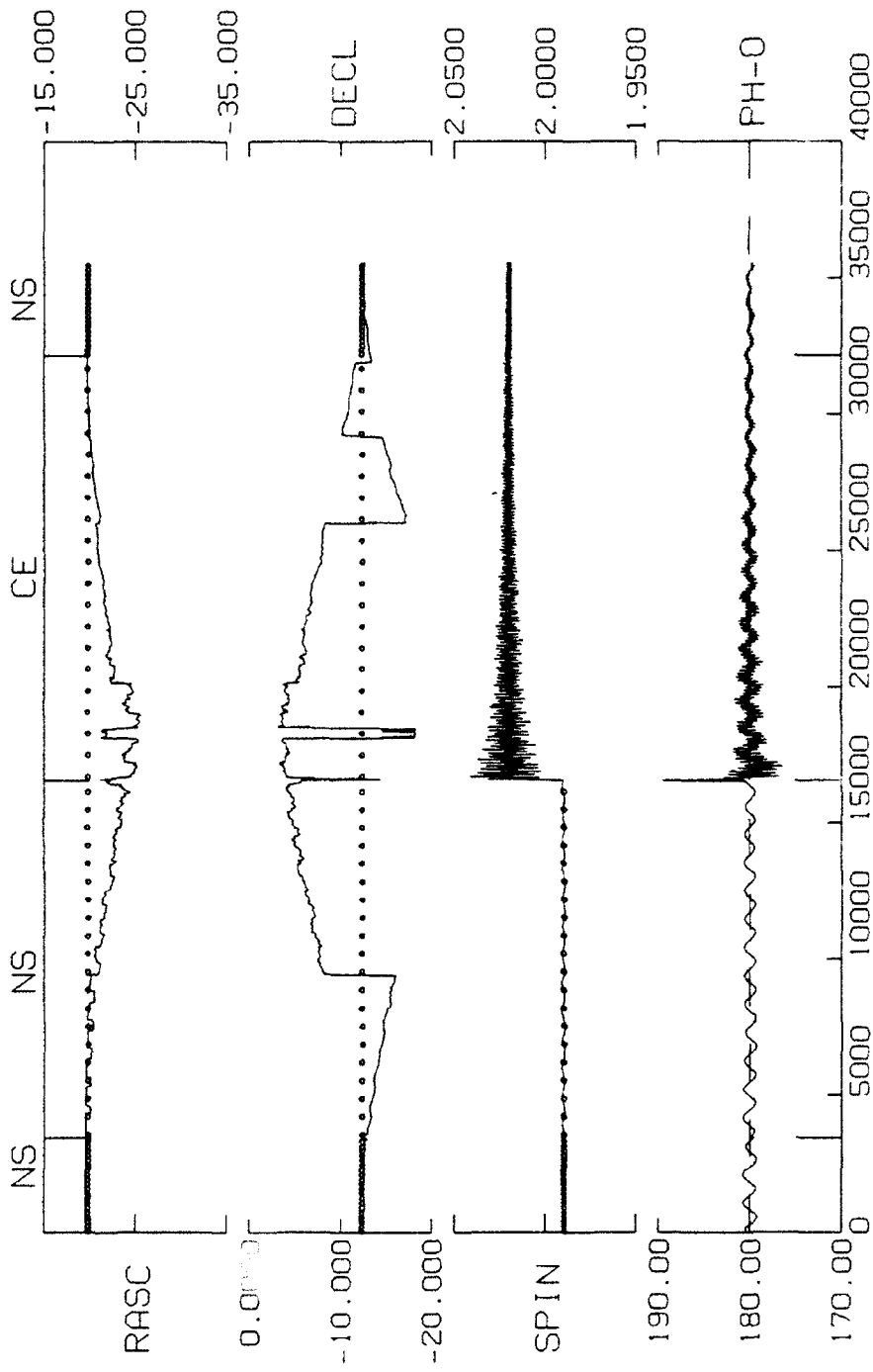
What we need	What we can measure	What we must estimate
Phase angles $\phi_x, \phi_y, \phi_z$	Phase differences $\phi_{xy}, \phi_{xz}$	Absolute x-sensor phase $\phi_x$
Elevations $\theta_x, \theta_y, \theta_z$	Ratios $T_{ij} = \tan\theta_i / \tan\theta_j$	Orthogonality angles $w_{ij}$
Gains $g_x, g_y, g_z$	Gain ratios $\gamma_{ij} = g_i / g_j$	Gain of x-sensor $g_x$
Offsets $d_x, d_y, d_z$	Spin-plane offsets $\Delta_1, \Delta_2$	Spin-axis offset $\Delta_3$

The inter-relationship between these quantities will become clear in what follows and this table is presented here mainly for reference. We reiterate that the quantities in the third column have all been calculated from on-orbit analysis during the course of the mission, or from ground measurements in the case of the  $w_{ij}$ 's. The calculation of these quantities will be described in the last sections of this work. In the sections immediately following, though, we will assume that these are known inputs to the calculations, in order to describe what came to be the routine orbit-by-orbit calibration and processing scheme for the CRRES magnetometer data.

#### 4.1. The Attitude

The vehicle attitude behavior during a particular orbit, which for CRRES, is defined as the period from one perigee pass to the next, is of central importance in calibration. Orbit-by-orbit calibration relies on the spacecraft maintaining more or less pure rotation about its z-axis, which in turn remains fixed in inertial space. Although slight changes in spin rate and/or spin axis direction do not disrupt the calibration scheme significantly, the changes that come at attitude and spin rate adjustments and at canister releases make it impossible to carry out routine calibration on those periods. For the most part, these periods were processed with calibration factors from previous orbits. It was necessary to know in advance when periods contained anomalies that would limit the effectiveness of calibration. For the purpose of determining when to calibrate, attitude plots like the one shown in Figure 1 were provided for each period. These

CRRES ADP ATTITUDE FROM CAF05020.  
 ORBIT 502 DAY 47 YEAR 1991 UTO 80880.00



29-SEP-92

Figure 1. Sample attitude quality control/survey plot.

plots were generated during attitude processing as a quality control device, but were quite sufficient as well in flagging periods which should not be calibrated.

The plots give the calculated right ascension and declination of the satellite in the top two panels, along with the model (dots) that will be used for despinning the data. The excursions of the solid line in those panels is a result of miscalibration and loss of resolution of the engineering magnetometer at apogee. It is near perigee that the data are of highest accuracy and the spin axis attitude is nearly constant throughout an orbit, as the dots of the model indicate. The third panel from the top gives the spin rate, again calculated and model values. The bottom gives the a quantity that is indicative of the accuracy of the attitude phase, but is exaggerated significantly in magnitude, due to error propagation from the spin axis inaccuracy. The phase angle of  $180^\circ$  is that of the sun sensor, along the negative x-axis of the spacecraft. Taken together, these panels can be used to locate attitude adjustments, spin ups and spin downs and various other events that affect calibration (Figure 1 shows a canister release). Reference to these plots can also give important clues to tracking down anomalies in the data itself, such as occasional discontinuities at segment boundaries, and may sometimes even allow for the differentiation between a real geophysical event and a spacecraft induced feature.

We have mentioned the attitude briefly here only because it is so ubiquitous to the calibration and processing of the magnetometer data from the outset. Knowing what to expect, orbit-by-orbit, from the satellite attitude aided immeasurably in the calibration process and in diagnosing data anomalies.

#### 4.2. Reduction to One-Second Data

The 16-sample/second data could have been used directly for calibration and despinning, however, this would have made for rather large and cumbersome data bases requiring substantial processing time. By averaging this data to a resolution of one second, we could reduce the size of the files and take advantage of the inherent reduction in noise. Also, except for infrequent events in which high time resolution data is of interest, a one or two second data base is sufficient for science study. Thus it was decided to perform calibration and despinning on once-per-second data and create a product data base at two-second resolution. Here again, 'one second' means 1.024 seconds approximately, the time being dependent on the frame rate. This section describes the steps taken to generate the one second data.

First, two full master frames of data are decoded from the telemetry format. Several checks are performed on the raw data in order to catch a number of anomalies. First, missing master frames, omitted in the CRRES data, are flagged by checking the time difference between successive master frames. These frames are filled in when encountered and flagged as bad data. 'Ones-filled' data, resulting from missing minor frames, are flagged by checking for values of negative one that result from the two's compliment evaluation of each 12-bit sensor value. This value in all three axes is taken to indicate a missing minor frame or a LASSII period, which is ones-filled as well in the GTO data files. A LASSII period is a time during which the satellite switches to low earth orbit experiments and the magnetometer is turned off. All points up to

3 seconds after the end of a period of ones-filling are discarded as well. A check is also carried out for off-scale readings and these are flagged as bad data when found. The x-sensor had a tendency to flip to high gain in a strong field from time to time, leading to this problem.

Next, a check is carried out to edit out 'Command Storage Memory' (CSM) mode, in which the data is actually a dump of the satellite memory instead of magnetometer readings. This mode is not explicitly indicated in the telemetry stream. This test looks for gain switches between subsequent samples in the data stream for the x-sensor. When an adjacent high and low gain sample are encountered, they are calibrated with nominal factors and their relative magnitude is compared. If the average of this difference is more than 1000 nT, the entire master frame is discarded. In addition, all points up to 13 seconds after a CSM dump are discarded. Finally, the magnetometer off condition is judged by a reading of zero for all three axes and is flagged. Bad data is carried through the processing and flagged in the product data bases.

Once all sensor readings have been edited, the 64 points from a master frame plus the first point from the following master frame are combined to form four one-second averages. Averages are created from seventeen sensor signals, which are left as counts but are floating point numbers, according to the following algorithm

$$\langle x(t_{MF} + 8\delta_{sf} + 16n\delta_{sf} - t_{delay}) \rangle = \frac{x_{1+n}}{32} + \frac{x_{2+n}}{16} + \frac{x_{3+n}}{16} + \dots + \frac{x_{16+n}}{16} + \frac{x_{17+n}}{32} \quad (2)$$

with  $n=0, 16, 32,$  and  $48$  and with  $x_{65}$  corresponding to the first sample of the next master frame.  $\delta_{sf}$  is the subframe rate of 0.128 seconds and  $t_{delay}$  is the delay time between sampling of the first magnetometer sample and the start of the major frame, 0.2225 seconds.

The fixed low gain samples, at frequency eight per major frame (one-half second) are also averaged according to

$$\langle x(t_{mf} + 8\delta_{sf} + 16n\delta_{sf} - t_{delay}) \rangle = \frac{x_{1+n}}{4} + \frac{x_{2+n}}{2} + \frac{x_{3+n}}{4} \quad (3)$$

with  $n=0, 2, 4,$  and  $6$  and again with  $x_9$  corresponding to the first sample from the next master frame. The fixed low gain average is flagged bad if *any* of the points that go into the average are flagged bad by the previous tests. Then, the seventeen points that go into the variable gain average are treated as follows:

- (a) If there are less than ten points present in a given set of 17 samples, the fixed low gain value is substituted for the variable gain average.
- (b) If the average requires mixing of gain states, the variable gain average is replaced by the fixed low gain average.
- (c) If the difference between any point and the average exceeds three times the standard deviation, the point is rejected and criterion (a) is reapplied.

These editing algorithms performed extremely well. After full implementation, the vast majority of the orbits came out with clean one-second data. Editing is especially important at this level because it is desirable to perform the bulk of the calibration as batch processing, where interactive editing is impossible. Further editing algorithms were in fact carried out on intermediate results of calibration. These will be discussed in the appropriate sections. We should mention that these processing steps are *not* carried out in the Time History Data Base magnetic field files. The 8-sample/second data there is not edited in any way.

There is a subtlety that should be mentioned relative to the creation of one-second averages. This effect, described fully in *McNeil and Singer* [1986] renders the modulation in the averages smaller than the true modulation by a small but significant factor. For the variable gain samples, the modulation in the average is smaller by a factor of

$$\chi_v = (1 + 2 \cos(\omega\tau) + 2 \cos(2\omega\tau) + \dots + 2 \cos(7\omega\tau) + \cos(8\omega\tau))/16 \quad (4)$$

and for the fixed low gain channels,

$$\chi_f = (1 + \cos(8\omega\tau))/2 \quad (5)$$

In Eq(4) and Eq(5),  $\omega$  is the spin rate and  $\tau$  is the spacing between points that were averaged (approximately 0.064 s). Correction for this effect is indeed made in the processing, but only after the signals have been converted to the spacecraft frame, when two components are pure modulation and the third is purely dc. In all other instances, these factors cancel in the calculations.

### 4.3 The Spin Fit

The basis quantity measured in on-orbit calibration is the modulated and dc portions of the magnetometer signal. Assuming that the external field is constant in time (we will remove this restriction later) and that the satellite spins at a uniform rate  $\omega$ , the signal from the  $i$ 'th sensor can be written as

$$s_i = g_i \cos\theta_i b_{xy} \cos(\phi_i + \omega t + \phi_b) + g_i b_z \sin\theta_i + d_i \quad (6)$$

where  $b_{xy}$  is the spin plane component of the external field,  $b_z$  is the spin axis component and  $\phi_b$  is the right ascension of the external field vector in spacecraft coordinates. Typical signals from the three sensors are shown in Figure 2. If we fit this signal to the functional form

$$s_i = \alpha_i \cos\omega t + \beta_i \sin\omega t + \delta_i \quad (7)$$

we can identify

$$\gamma_i = \sqrt{(\alpha_i^2 + \beta_i^2)} \quad (8)$$

# CRRES Magnetometer Sensors --- Orbit 587

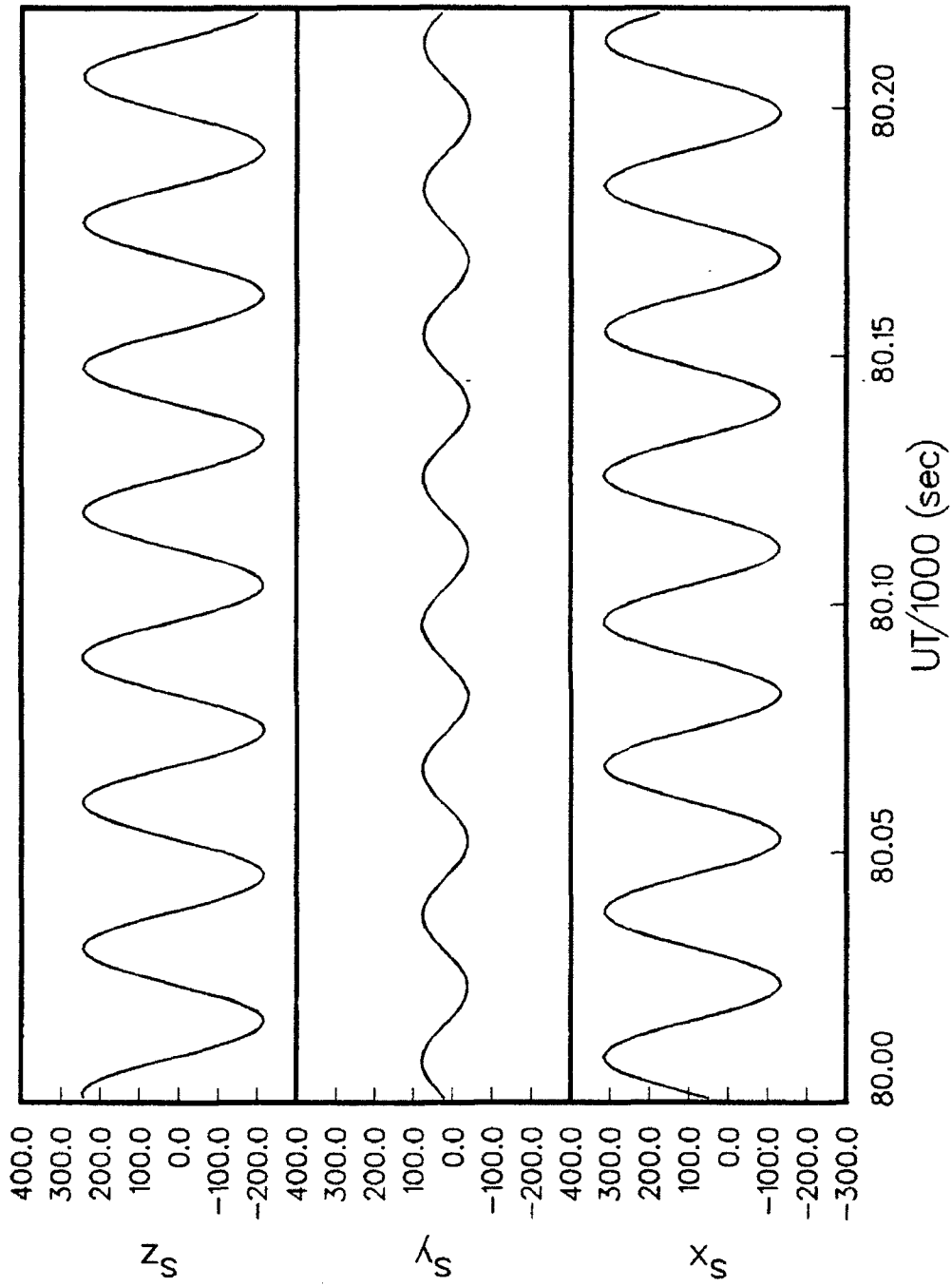


Figure 2. Sample sensor signals from low field.

as the modulated component of the signal and  $\delta_i$  as the dc component. Further, we see that

$$\tan^{-1} \frac{\beta}{\alpha} = \phi_b - \phi_i \quad (9)$$

In our calibration software, we allow the external field to be a polynomial of arbitrary order in time, leading to a fitting function of the form

$$s_i = \delta_1 + \delta_2 t + \dots + \delta_n t^n + (\alpha_1 + \alpha_2 t + \dots + \alpha_n t^n) \cos \omega t + (\beta_1 + \beta_2 t + \dots + \beta_n t^n) \sin \omega t \quad (10)$$

In all cases, though, all terms but  $\delta_1$ ,  $\alpha_1$ , and  $\beta_1$  are discarded. It is from these spin fit results, taken at various times throughout the CRRES orbit, that the results of calibration are obtained. In routine processing, the linear representation of the field proved to be optimum for calibration.

The signals are fit by least squares over an interval of 60-seconds, or approximately two spins. The least squares equation can be solved analytically for this model. The system reduces to a set of linear equations which, for the constant ( $n=1$ ) case is given by

$$\begin{bmatrix} \sum \cos^2 \omega t_i & \sum \cos \omega t_i \sin \omega t_i & \sum \cos \omega t_i \\ \sum \cos \omega t_i \sin \omega t_i & \sum \sin^2 \omega t_i & \sum \sin \omega t_i \\ \sum \cos \omega t_i & \sum \sin \omega t_i & \sum 1 \end{bmatrix} \begin{bmatrix} \alpha_1 \\ \beta_1 \\ \delta_1 \end{bmatrix} = \begin{bmatrix} \sum s_i \cos \omega t_i \\ \sum s_i \sin \omega t_i \\ \sum s_i \end{bmatrix} \quad (11)$$

The least squares matrix is inverted with the routine INVDET [Hornbeck, 1975]. Because the high and low gain calibration factors may be different, fits are performed only when all samples for all three sensors are in the same gain state. An exception is when there is a single high gain sample with low gain on either side. This happens frequently when the signal passes through zero. In that case, the fixed low gain sample is substituted for the variable gain sample for the single second. Fit coefficients are produced at one-minute intervals throughout the orbit. Whenever a full minute of good data is available, a low gain set is always produced using either the variable gain samples or, if the variable gain channels are mixed or in high gain, the fixed low gain channels. High gain fit coefficients are produced only if the variable gain channels are completely in high gain. After fitting, the  $\gamma_i$  values are calculated from Eq(8) and the relative phases of the sensors are calculated from Eq(9).

#### 4.4. The Calculation of Alignments

In the CRRES calibration system, the alignments are calculated first. We have developed three more or less independent methods for the calculation of the alignments. The first of which is the most complicated. Since this method appeared to be the most stable in practice, it was used throughout the processing.

Before we begin, we note that we cannot hope to calculate the phases in Eq(1) from spin fit data alone. Thus, we define a relative alignment matrix  $A$  as representing the phases relative to the phase of the x-sensor. The object of this section will be to calculate the components of  $A$ . Once we have these, supplemental analyses can be used to transform  $A$  into the matrix of Eq(1) and thus arrive at an equation by which the sensor signals can be transformed back into the spacecraft frame. Since the spacecraft attitude is expressed as the vectors of the spacecraft axes in the inertial frame, this is all we will need for despinning the data.

$$A = \begin{bmatrix} \cos\theta_x & 0 & \sin\theta_x \\ \cos\theta_y \cos\phi_{xy} & \cos\theta_y \sin\phi_{xy} & \sin\theta_y \\ \cos\theta_z \cos\phi_{xz} & \cos\theta_z \sin\phi_{xz} & \sin\theta_z \end{bmatrix} \quad (12)$$

After the spin fit has been performed, the fit coefficients are converted into intermediate quantities. These quantities are averaged over selected portions of the orbit. For typical runs, the calculations are limited to magnetic field values between 300 nT and 5000 nT. The phases obtained from the fits are converted to phase relative to the x-sensor through

$$\phi_{xy} = \phi_x - \phi_y \quad \phi_{xz} = \phi_x - \phi_z \quad (13)$$

Figure 3 shows one of the relative phases. The plot shown is from the editing screen of the processing system. This editing is optionally available when calibration is done in interactive mode. The ratios

$$\gamma_{ij} = \frac{\gamma_x}{\gamma_y} = \frac{g_i \cos\theta_i}{g_j \cos\theta_j} \quad (14)$$

are computed and averaged. Figure 4 shows typical results. Linear regression is carried out on the  $\delta_i$  values to obtain the quantities

$$\delta_{ij} = \frac{d(\delta_i)}{d(\delta_j)} = \frac{g_i \sin\theta_i}{g_j \sin\theta_j} \quad (15)$$

Figure 5 shows one such typical calculation.

The first method of alignment calculation takes as input the values of  $\gamma_{ij}$  and of  $\delta_{ij}$ . It requires the sensor orthogonalities  $w_{ij}$  and returns both the elevations  $\theta_i$  and the relative phases  $\phi_{ij}$  of the sensors. We analyzed measurements by Schonstedt to arrive at the sensor orthogonalities given in Table 2. These angles are defined as the angles between the sensor axes.

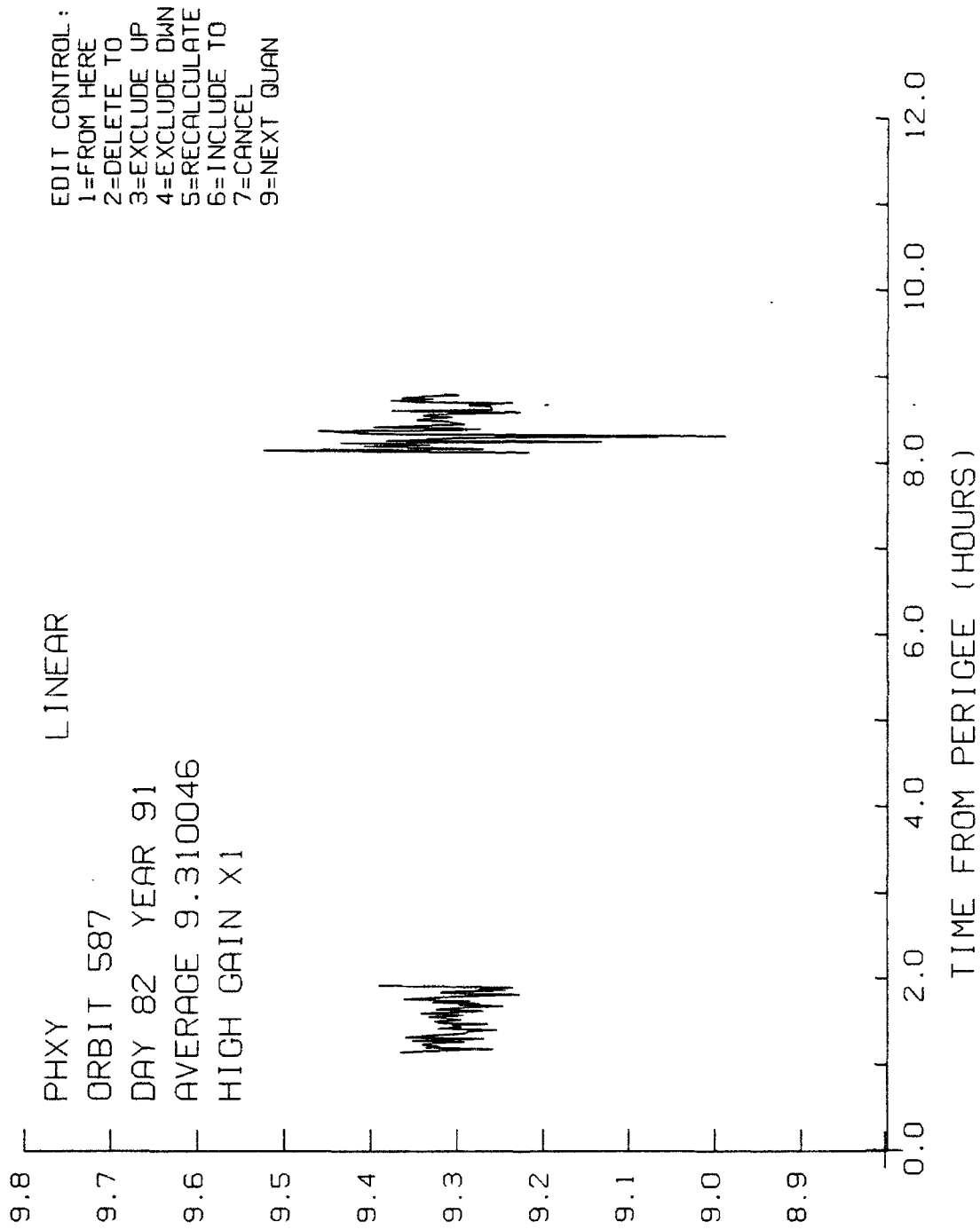


Figure 3. Calculated relative sensor phase  $\phi_{ij}$ .



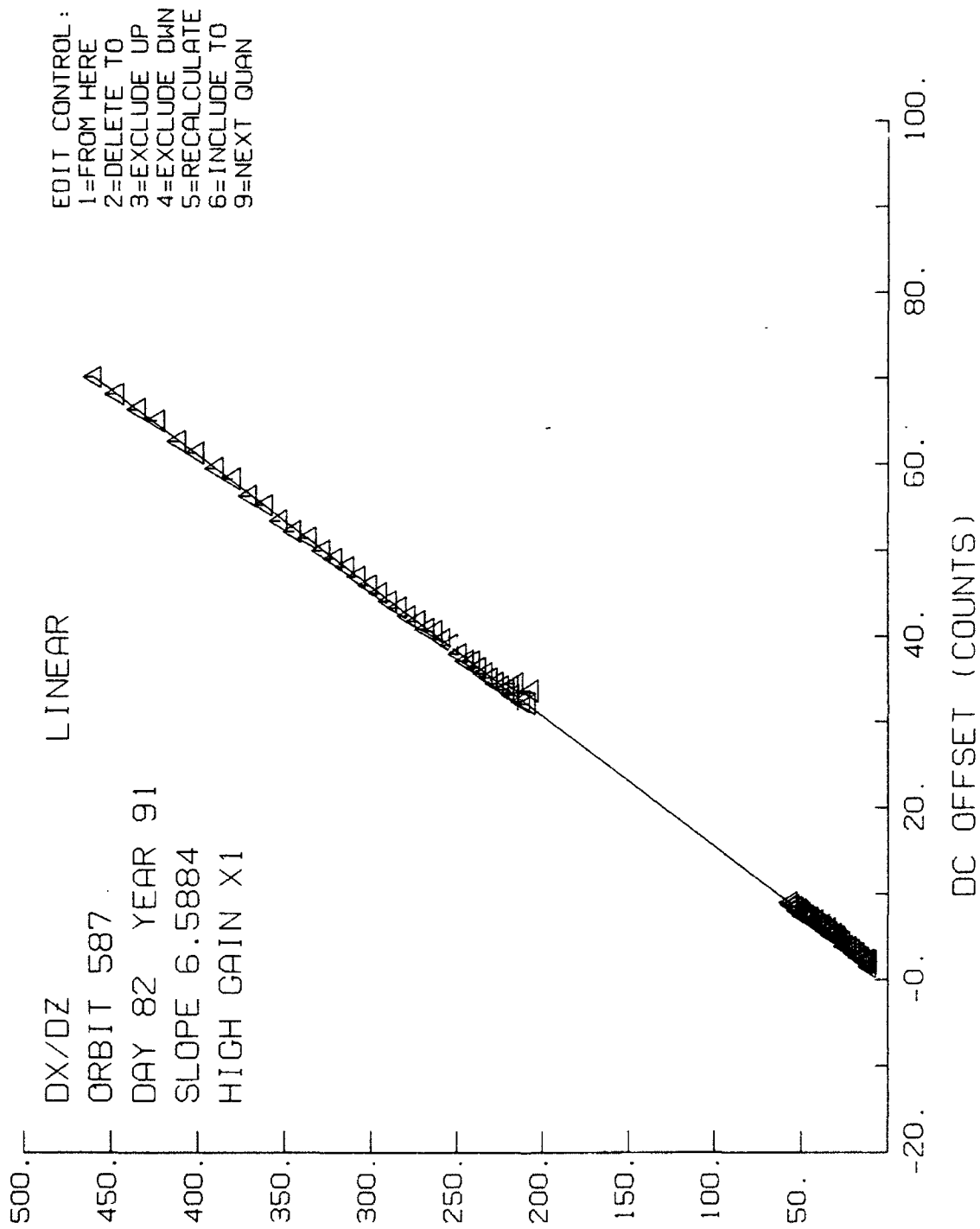


Figure 5. Calculated gain modified elevation sine ratio  $\delta_{ij}$ .

**Table 2. Sensor Orthogonality**

$w_{xy}$	90.0033°
$w_{xz}$	90.0113°
$w_{yz}$	90.0219°

In this method, the alignment matrix in Eq(12) is first recast into a coordinate system in which  $\phi_x$  is zero and in which the values of the other five alignment angles are represented completely by the three orthogonality angles  $w_{ij}$  and two rotation angles  $\kappa$  and  $\mu$ . The vector directions of the sensor axes are then given by

$$S(w_{xy}, w_{xz}, w_{yz}, \kappa, \mu) = Q(w_{xy}, w_{xz}, w_{yz})R(\kappa, \mu) \quad (16)$$

Now, we derive an orthogonal coordinate frame, the OM frame, in which the rotations about  $\kappa$  and  $\mu$  are defined. Further, in this system, the x-sensor is co-linear with the  $x_{OM}$  axis and the y-sensor is in the  $xy_{OM}$  plane. The elements of the Q matrix are given by

$$(Q)_{ij} = m_i \cdot j_{OM} \quad (17)$$

where  $m_i$  is the i-sensor direction and  $j_{OM}$  is the direction of j-th coordinate axis. First, by definition, we have

$$m_x \cdot i_{OM} = 1 \quad m_x \cdot j_{OM} = m_x \cdot k_{OM} = 0 \quad (18)$$

The position of the  $m_z$  axis is found through the relations

$$m_x \cdot m_z = w_{xz} \quad m_y \cdot m_z = w_{yz} \quad m_z \cdot m_z = 1 \quad (19)$$

and the result is

$$Q = \begin{bmatrix} 1 & 0 & 0 \\ \cos w_{xy} & \sin w_{xy} & 0 \\ \cos w_{xz} & \cos c & \cos d \end{bmatrix} \quad (20)$$

where

$$\cos d = \sqrt{1 - \cos^2 w_{xy} - \cos^2 c} \quad (21)$$

and

$$\text{cosc} = (\text{cos}\omega_{yz} - \text{cos}\omega_{xy}\text{cos}\omega_{xz}) / \text{sin}\omega_{xy} \quad (22)$$

Eq(20) can be verified by noting that it satisfies Eq(19).

Next, we find the alignment matrix **R**. This matrix includes the sign inversion and the  $y \leftrightarrow z$  inversion [McNeil and Singer, 1986] that exists in the nominal mounting of the instrument. Following this is a negative (clockwise) rotation about the spacecraft x-axis by the angle  $\kappa$  and a positive (counter-clockwise) rotation around the spacecraft y-axis by the angle  $\mu$ . Roughly speaking,  $\kappa$  is angle by which the y-sensor is tilted with respect to the spin axis and  $\mu$  is the negative of the elevation of the x-sensor above the spacecraft plane. Nominally aligned,  $\kappa$  is  $2.5^\circ$  and  $\mu$  is zero. The **R** matrix is given by

$$R(\kappa, \mu) = \begin{bmatrix} -\text{cos}\mu & 0 & \text{sin}\mu \\ -\text{sin}\mu \text{cos}\kappa & -\text{sin}\kappa & -\text{cos}\mu \text{cos}\kappa \\ \text{sin}\mu \text{sin}\kappa & -\text{cos}\kappa & \text{cos}\mu \text{sin}\kappa \end{bmatrix} \quad (23)$$

These two matrices are multiplied to define the alignment matrix equivalent to Eq(12) (again with phase angles measured relative to that of the x-sensor) but which has only two unknowns,  $\kappa$  and  $\mu$ . We can choose any two sensors ratios  $T_{ij}$  with which to perform the calculation, since we find the results are more or less the same. Choosing

$$T_{xy} \equiv \frac{\tan\theta_x}{\tan\theta_y} = \frac{\gamma_{xy}}{\delta_{xy}} \quad T_{xz} \equiv \frac{\tan\theta_x}{\tan\theta_z} = \frac{\gamma_{xz}}{\delta_{xz}} \quad (24)$$

we find solutions to the equations

$$F = \frac{\tan\theta_x(\kappa, \mu) / \tan\theta_y(\kappa, \mu) - T_{xy}}{T_{xy}} \quad G = \frac{\tan\theta_x(\kappa, \mu) / \tan\theta_z(\kappa, \mu) - T_{xz}}{T_{xz}} \quad (25)$$

giving us results for  $\kappa$  and  $\mu$ .  $T_{ij}$  is included in the denominator to compensate for the differing magnitudes of  $T_{xy}$  and  $T_{xz}$ . As a function of  $\kappa$  and  $\mu$ , we chose to express the values of  $\theta_i$  by the spin axis components, *i.e.*

$$\begin{aligned} \sin\theta_x &= Q_{11}R_{13} + Q_{12}R_{23} + Q_{13}R_{33} \\ \sin\theta_y &= Q_{21}R_{13} + Q_{22}R_{23} + Q_{23}R_{33} \\ \sin\theta_z &= Q_{31}R_{13} + Q_{32}R_{23} + Q_{33}R_{33} \end{aligned} \quad (26)$$

The solution is found through two-dimensional Newton-Raphson with the derivatives evaluated numerically. The starting point is taken at  $\kappa=2.5^\circ$  and  $\mu=15^\circ$ .

$$\begin{bmatrix} \kappa \\ \mu \end{bmatrix}^{(i+1)} = \begin{bmatrix} \kappa \\ \mu \end{bmatrix}^{(i)} - \begin{bmatrix} dF/d\kappa & dF/d\mu \\ dG/d\kappa & dG/d\mu \end{bmatrix}^{-1} \begin{bmatrix} F \\ G \end{bmatrix}^{(i)} \quad (27)$$

Once values for  $\kappa$  and  $\mu$  are obtained, Eq(12) is used to find the values  $\phi_{ij}$ .

$$\phi_{xy} = \tan^{-1} \frac{\sum_{j=1,3} Q_{2j} R_{j2}}{\sum_{j=1,3} Q_{2j} R_{j1}} - \pi \quad \phi_{xz} = \tan^{-1} \frac{\sum_{j=1,3} Q_{3j} R_{j2}}{\sum_{j=1,3} Q_{3j} R_{j1}} - \pi \quad (28)$$

where  $\pi$  has been subtracted since  $\phi_x$  is  $\pi$  in Eq(23). It is important that these values for  $\phi_{ij}$  be used for despining *instead* of those calculated in Eq(13) since this preserves the sensor orthogonality. It is also important that the self-consistent result for  $\theta_{ij}$  be used in the subsequent analysis and despining, rather than any sort of average values.

Now, this is all rather complicated, but it has the benefit that it incorporates all three sensor orthogonality angles and preserves orthogonality. Recognizing the complexity of the scheme, we developed two other more or less independent methods with which the results could be compared. The first uses a single orthogonality angle from any one sensor pair (we chose  $w_{xy}$  since it gives better results in this calculation, which is quite sensitive to that choice). An initial guess is made for  $\theta_x$ . Then, the value of  $\theta_y$  is calculated from

$$\cos\theta_y = \frac{\cos\theta_x}{\gamma_{xy}} \left[ \frac{\gamma_{xy}}{\cos^2\theta_x} + \frac{\delta_{xy}}{\sin^2\theta_x} \right]^{\frac{1}{2}} \quad (29)$$

where the term in (..) was added to ensure normalization of the result. The angle between the two is then calculated from

$$\cos w_{yz} = \cos\theta_y \cos\theta_z \cos\phi_{yz} + \sin\theta_y \sin\theta_z \quad (30)$$

The calculation continues until the value of  $w_{yz}$  matches the assumed value, the guess for  $\theta_z$  being modified in the direction consistent with Eq(30). After the desired value of  $\theta_y$  has been determined,  $T_{xy}$  is used to calculate  $\theta_x$  directly. This method resulted in elevations that were in very good agreement with that of the  $\kappa$  and  $\mu$  method presented above. It suffers, however, in that it does not necessarily preserve the orthogonality of the sensor arrangement, which for CRRES was extremely orthogonal. This results in a bit more spin tone in the despun results.

A third method relies on knowledge of the gain ratio between two of the sensors. We find it best to use  $r_{yz} \equiv g_y/g_z$ . Guessing a value for  $\theta_z$ , we calculate

$$r_{yz}^2 = \gamma_{yz}^2 \cos^2 \theta_z + \delta_{yz}^2 \sin^2 \theta_z \quad (31)$$

We modify the value of  $\theta_z$  until it matches the assumed gain ratio  $r_{yz}$ . Then  $\theta_y$  is found from

$$\cos \theta_y = \gamma_{yz} \cos \theta_z / r_{yz} \quad (32)$$

and similarly for  $\theta_x$ . Usually, the first two of these methods will agree to better than  $0.01^\circ$  in the elevations of the sensors. The third method, tends to exhibit larger deviations of perhaps  $0.1^\circ$  in calculations performed on the same data set. From orbit to orbit, the calculation gives results that are consistent to about  $0.2^\circ$ , as shown in Figure 6, where the six alignment variables used in the final processing of the data are presented. Figure 6 reiterates that the value of  $\phi_x$  is not calculated but rather is supplied as an assumed input and is therefore constant throughout. About half-way through the processing, we discovered that angular agreement with model field data was considerably better if this phase angle was set nearer to  $177.5^\circ$ . We reasoned that this resulted from the miss-deployment and made provisions to adjust all the processed data by this angular difference.

The noise in Figure 6 is probably indicative of the absolute pointing direction error in the magnetometer data, about one-quarter degree maximum. As we will see in the next section, the remainder of the calibration seeks mostly to adjust offsets and gain ratios to remove spin tone, all based on these input alignments. Because of this, it is important that alignments and gains be considered as a unit during processing, instead of mixing gains from one calibration with alignments from another.

The jump between Orbit 416 and Orbit 421, especially noticeable in  $\phi_y$ , is most likely due to a real displacement of the spin axis in the body frame resulting from weight redistribution from canister releases. This points out an important aspect of the alignment calculation. The algorithm gives alignments relative to the *actual* spin axis of the satellite and not the nominal spin axis. The difference between these two, the wobble angle, is an inherent limitation on the accuracy of the spacecraft frame field vector. The magnitude of the change in any one variable in Figure 6 is not necessarily indicative of the magnitude of the wobble. However, one can safely infer that the *change* in the wobble angle during this release campaign was no more than a few tenths of a degree.

Finally, we note that this entirely general method of alignment calculation allowed us to deal quite easily with the misdeployment of the instrument and, in fact, allowed us to watch the gradual 'stretching out' of the boom as time progressed. The x-sensor elevation was almost  $18^\circ$  at deployment, it was about  $15^\circ$  by orbit 50 when routine processing began and it decreased almost linearly to  $14^\circ$  by about orbit 350. This motion, echoed in the other sensors as well, is consistent with the gradual stretching of whatever was holding up the boom deployment.

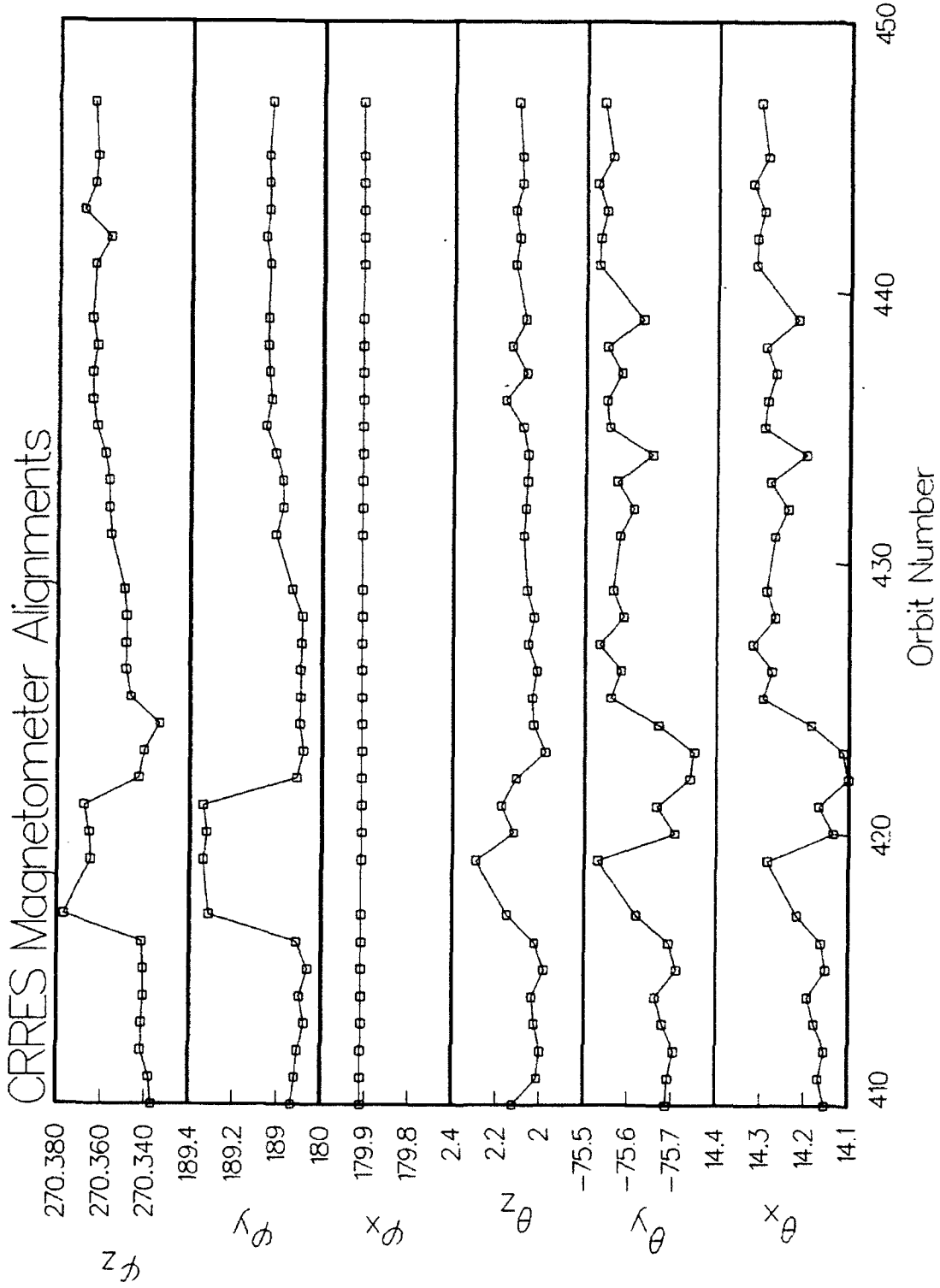


Figure 6. Alignments calculated for Orbits 410-450.

#### 4.5. The Calculation of Gain Ratios

With the alignments calculated in §4.4, we can use either the  $\gamma_{ij}$  or the  $\delta_{ij}$  values to obtain the ratios of the gains between the sensors. For the low gain signals, however, a slightly different approach was found to give improved results. If we plot, for example,  $\gamma_{xl}/\cos\theta_x$  against  $\gamma_{yl}/\cos\theta_y$ , the slope yields the gain ratio between x and y sensors in low gain;  $r_{xyl}$ . (The subscript l or h will be added from this point onward to indicate low or high gain respectively.) Figure 7 shows an example of this calculation from the edit screen of the processing system. The calculations are, by default, carried out in field strengths between 500 nT and 9000 nT. For high gain signals, the ratios are calculated from, for example,

$$r_{xz} = \frac{\gamma_x \cos\theta_z}{\gamma_z \cos\theta_x} \quad (33)$$

Figure 8 shows a typical calculation, which is carried out between 300 nT and 800 nT by default.

A third set of ratios calculated is the ratio of the i'th sensor in low gain to the same sensor in high gain. This calculation uses the averaged sensor signals  $s_i$  instead of the results of the spin fitting. In this calculation, the offsets are subtracted and 60-second summations are taken. The signals are corrected by  $\chi_v$  and  $\chi_f$  from §4.2 and plotting one against the other yields a value for  $r_{xlh}$ ,  $r_{yly}$  and  $r_{zly}$ . In calibration, the gains and offsets are calculated in tandem. In the first pass, offsets are calculated with nominal gain ratios and are used to calculate the low to high gain ratios. On the second pass, the results of the first pass are used to calculate offsets. Since the offset calculation requires  $r_{xy}$  and  $r_{yz}$ , which do not themselves require offsets for their calculation, convergence is obtained on the second pass. From Eq(6), the x-sensor low gain term, for example, is

$$x_l = g_{xl} \sum_i (\cos\theta_x b_{xy,i} \cos(\phi_x + \omega t_i + \phi_{b,i}) + b_{z,i} \sin\theta_x) \quad (34)$$

Since the summation is identical for high and low gain, the slope yields the ratio. Figure 9 shows one such calculation. These calculations are carried out whenever a full minute of variable gain sensor data is in high gain *and* when the field is larger than 200 nT.

The values of gain ratios in low gain calculated above were quite adequate for offset calculations, however, we developed a way to improve the ratios at the end of the iterative calculation. In this method, the offsets are subtracted from 300 seconds of low gain data. Then, these are normalized by multiplication of  $s_y$  by  $r_{xy}$  and  $s_z$  by  $r_{xz}$ . These are then converted into the spacecraft frame. Since a gain mismatch will show up in both the values of the spin axis field  $b_z$  and the spin plane field  $b_{xy}$ , a good measure of the miss-match is given by the quantities

$$F(r_{xy}, r_{yz}) = \sum (R_z \cdot s - \langle R_z \cdot s \rangle)^2 \quad (35)$$

and

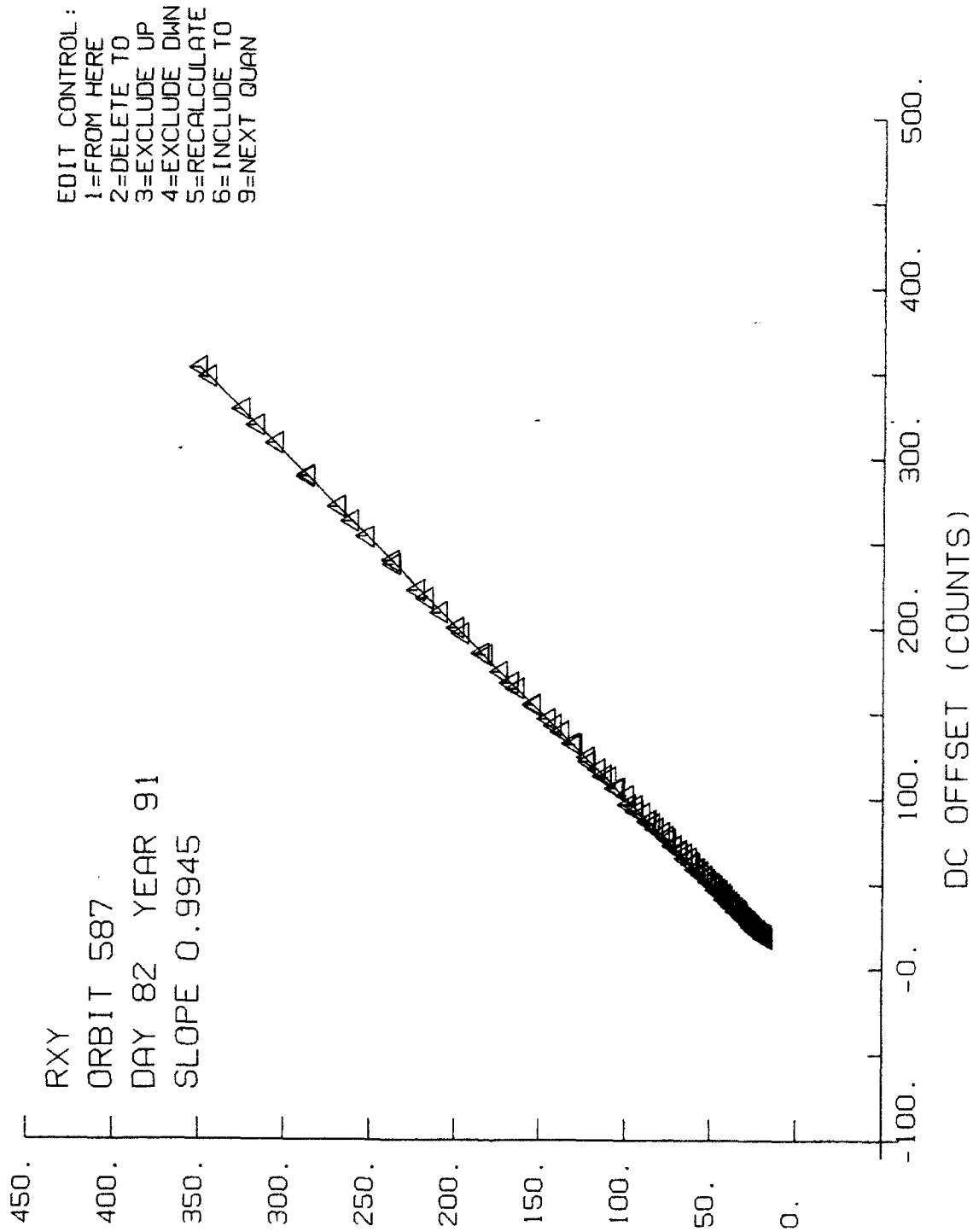
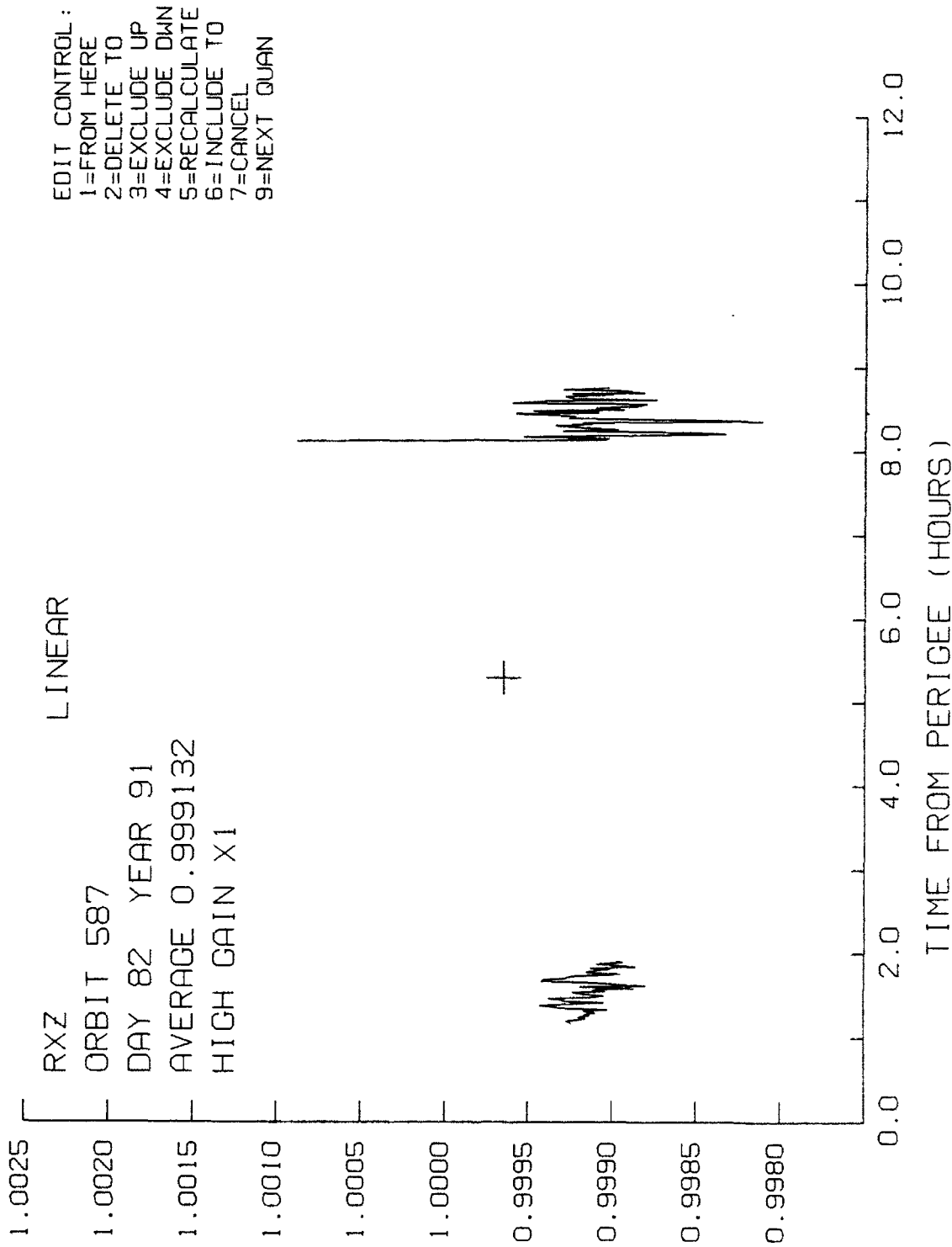


Figure 7. Calculated low gain ratio of y-sensor to x-sensor gains.



**Figure 8.** Calculated high gain ratio of x-sensor to z-sensor gains.

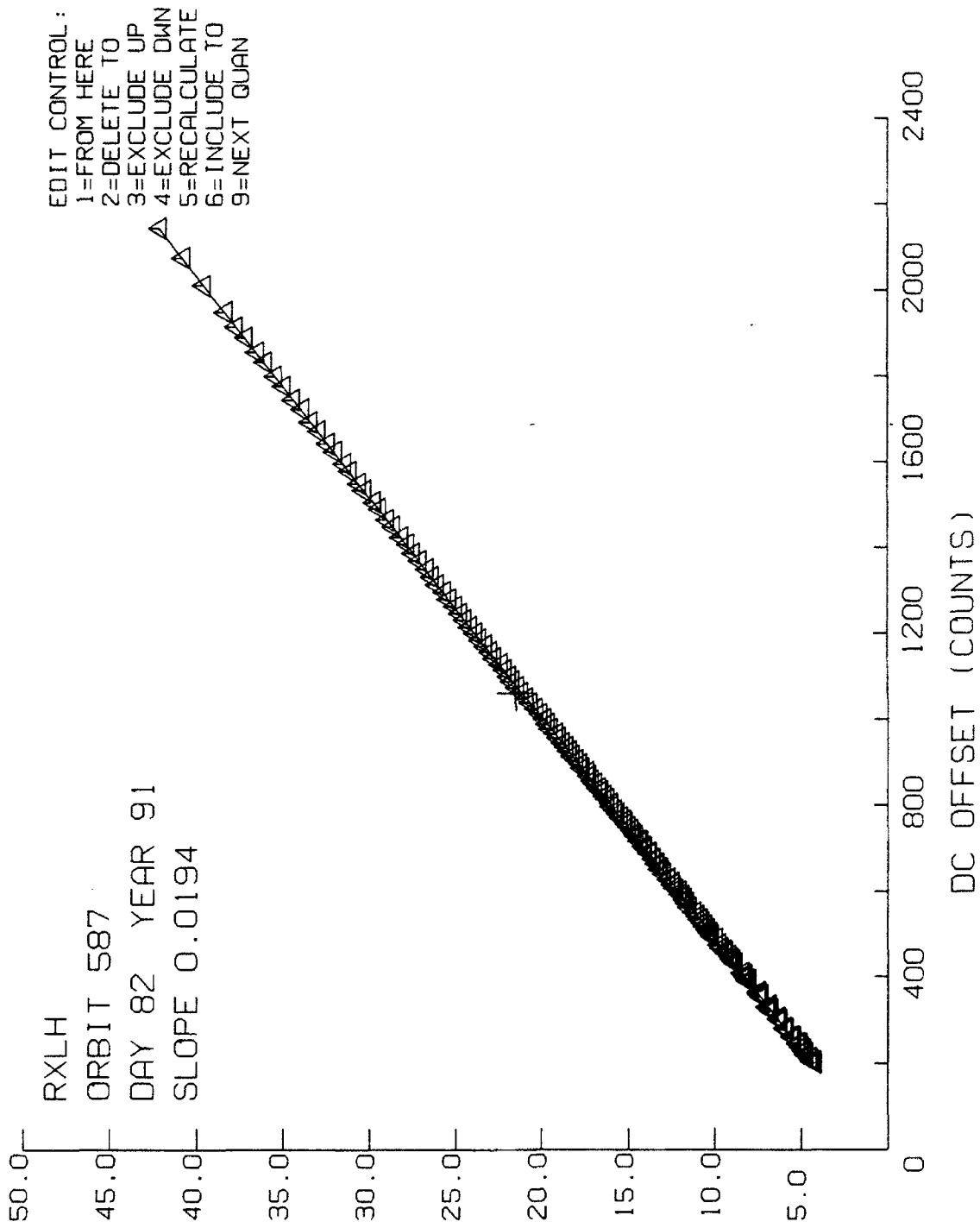


Figure 9. Calculated ratio between low to high gain in the x-sensor.

$$G(r_{xy}, r_{xz}) = \sum ([(R_x \cdot s)^2 + (R_y \cdot s)^2]^{1/2} - \langle [(R_x \cdot s)^2 + (R_y \cdot s)^2]^{1/2} \rangle)^2 \quad (36)$$

and where

$$s = (s_x - d_x, r_{xy}(s_y - d_y), r_{xz}(s_z - d_z)) \quad (37)$$

$R_i$  in Eq(35) and Eq(36) is the  $i$ 'th row of the alignment matrix in Eq(12). In essence,  $F$  and  $G$  are simultaneously minimized with respect to  $r_{xy}$  and  $r_{xz}$ . The averaged values of these functions in  $\langle \dots \rangle$  are calculated from 30 point running averages, which average out the external field, so that when  $F$  and  $G$  approach zero, the spin tone also approaches zero. The minimization was done by a routine called AMOEBA [Press, *et al.*, 1986]. The calculation was carried out on all sets of 300 seconds for which the field was stronger than 5000 nT.

#### 4.6. Calculation of Offsets

For both high and low gain states, linear combinations are made of the measured  $\delta_i$  values as follows:

$$\begin{aligned} \Delta_1 &= \sin\theta_x \delta_y - r_{xy} \sin\theta_y \delta_x \\ \Delta_2 &= \sin\theta_z \delta_y - r_{yz} \sin\theta_y \delta_z \end{aligned} \quad (38)$$

Eq(6) can be used to show that these expressions are independent of the external field component  $b_z$ . These are averaged throughout the entire data set, in both low and high gain. To them, is added the equation

$$\Delta_3 = \sin\theta_x d_x + \sin\theta_y d_y + \sin\theta_z d_z \quad (39)$$

where  $\Delta_3$  is the quantity supplied to the calculation. We could have defined  $\Delta_3$  in almost any way, as long as it was linearly independent of  $\Delta_1$  and  $\Delta_2$ . Although the 'spin axis offset' is a rather nebulous term, what we have defined as  $\Delta_3$  is the vector sum of the offset produced along the spin axis by biases in the three sensors. We will find that this is equal to the result of our bias calculation, discussed later. So, the definition of Eq(39) is a convenient choice. At this point, we assume that we have a value of  $\Delta_3$  for both high and low gain, which may have come either from a bias calculation or from ground measured values of  $d_x$ ,  $d_y$  and  $d_z$  and Eq(39). These three equations make the linear matrix equation

$$\begin{bmatrix} \Delta_1 \\ \Delta_2 \\ \Delta_3 \end{bmatrix} = \begin{bmatrix} \sin\theta_y & -r_{xy}\sin\theta_x & 0 \\ 0 & \sin\theta_z & -r_{yz}\sin\theta_y \\ \sin\theta_x & \sin\theta_y & \sin\theta_z \end{bmatrix} \begin{bmatrix} d_x \\ d_y \\ d_z \end{bmatrix} \quad (40)$$

In calibration, the averaged values of  $\Delta_1$  and  $\Delta_2$  are used, the matrix is inverted and values for the orbit averaged offsets  $d_i$  result.

Figure 10 shows the once-per minute values for  $\Delta_1$ , calculated directly from individual spin fits. As can be seen, there are factors which appear to change the offset within an orbit. For general use, the four count, or about 2 nT, variation within an orbit is not really troublesome, since it amounts to a maximum of about 1° error in the direction of the field. This is generally less than the mounting accuracy and the apertures of the particle instruments. However, this error does induce spin tone of approximately the same magnitude, *i.e.* 2 nT, in the despun magnetic field. This is an annoyance for display of the data and interferes with low frequency spectra. We were able to improve on the result by calculating 'instantaneous' offsets from the results of individual spin fits, once per minute. Then these were averaged over intervals, usually 5 minutes, to be used for despinning. Figure 11 shows a typical 5-minute averaged offset plot. One can see from this plot that the values of  $d_x$  and  $d_y$  do appear very similar in behavior. This is because the value of  $\Delta_1$  contributes mostly to  $d_x$  and  $d_y$ , along with the value of  $\Delta_3$ , held constant throughout the calculation.  $d_z$  on the other hand comes almost entirely from  $\Delta_2$ . The plot in Figure 11 was routinely generated for all orbits processed and can be used to verify the soundness of the calibration as well as the behavior of the offsets themselves. The offset changes at the beginning and end of the orbit probably result from heating and cooling due to eclipses. The two large changes near the middle are a result of the power amplifier operation.

#### 4.7. The Calculation of Gains

With the gain ratios in hand, and assuming knowledge of one of the gains (we assume  $g_{xh}$ ), there are several ways to find the other five gain values, all of which would yield slightly different results. The method we find to be the best at reducing spin tone is the following.

$$g_{yh} = g_{xh}/r_{xyh} \quad g_{zh} = g_{xh}/r_{xzh} \quad g_{xl} = g_{xh}/r_{xlh}$$

$$g_{yl} = g_{xl}/r_{xyl} \quad g_{zl} = g_{xl}/r_{xzl}$$

Then, using

$$\phi_y = \phi_x - \phi_{xy} \quad \phi_z = \phi_x - \phi_{xz} \quad (42)$$

we have a full set of 12 calibration factors to substitute into Eq(1). This equation is then solved for the spacecraft frame magnetic field  $\mathbf{b}$ . The only thing left to do is to transform this measured field into an inertial frame, which requires the satellite attitude and which will be discussed in a later section in the context of the product data bases.

### 5. Calculation of the Assumed Quantities

In the preceding section, we described how the twelve quantities needed for conversion of the sensor measurements to the spacecraft frame magnetic field values were calculated from on-orbit measurements along with the assumed quantities, the angles between the sensors  $w_{ij}$ , the spin axis bias  $\Delta_3$ , the gain of the x-sensor in high gain,  $g_{xh}$  and the phase of the x-sensor  $\phi_x$ .



Calculated H.G. Offsets — Orbit 1010 260/91 5 Pt. Ave.

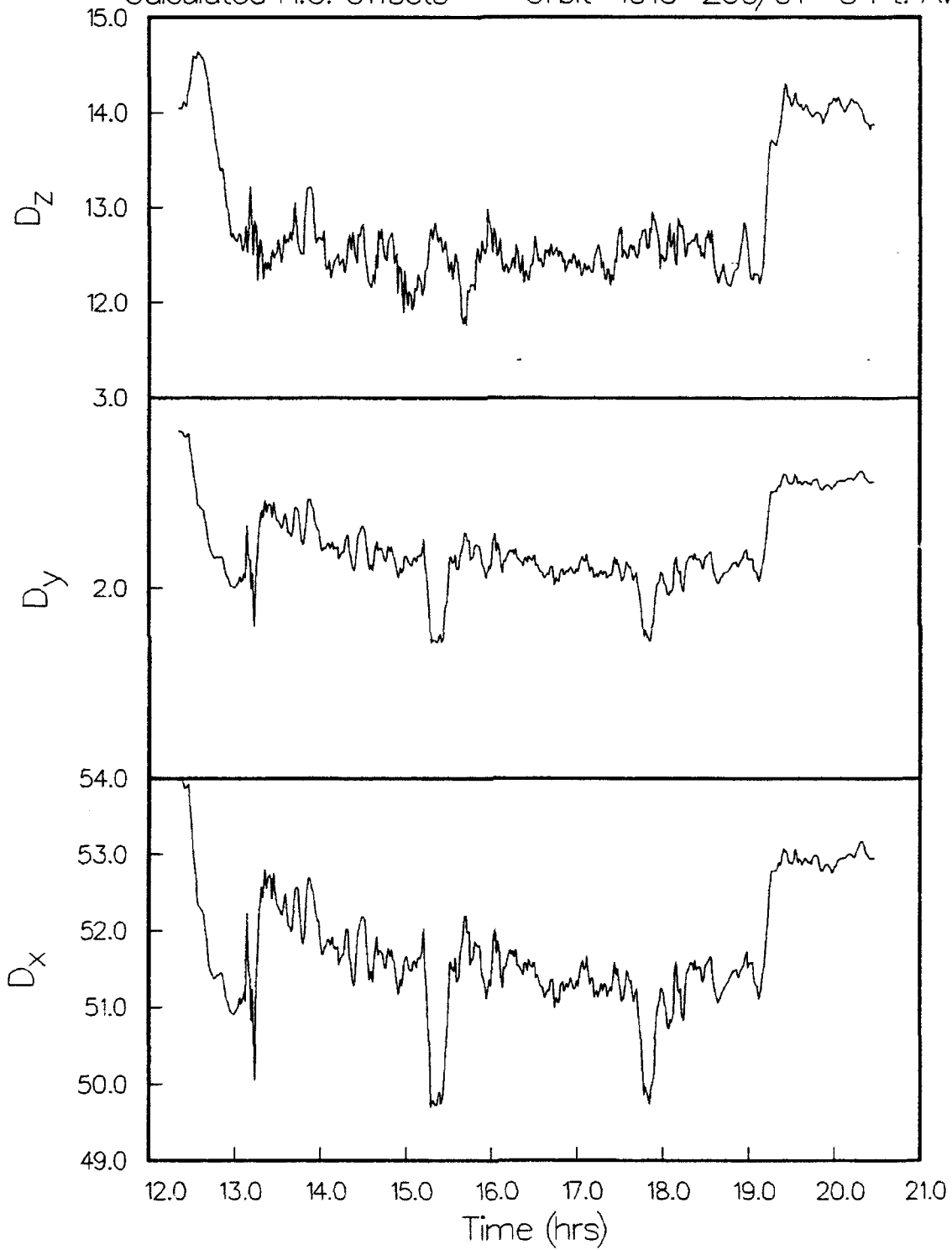


**Figure 11.** Calculated 5-minute averaged sensor offsets in high gain.

These calculations were carried out routinely on nearly every orbit, the exceptions being those where attitude maneuvers made spin fits impossible. The three assumed quantities were in fact computed in the processing, although not for every orbit. This section describes the computation of those quantities.

### 5.1. The Calculation of $\Delta_3$

The calculation of  $\Delta_3$  relies on motion of the spacecraft spin axis in relation to the external field. Originally, a precession maneuver was planned especially for this purpose. The maneuver was performed, but ultimately over a much smaller angle than originally specified. The data resulting from this maneuver was not of much use in the calculation. Fortunately, though, there was a 'natural' motion of the spin axis, the nutation of the spin axis induced by attitude adjustments which were performed about every ten days or so. These data turned out to work quite nicely in the calculation.

The algorithm requires two separate calculations, one quite similar to the calculation of offsets in §4 and giving the spin plane offsets which we will call  $D_x$  and  $D_y$ . This calculation was carried in periods when there was no motion of the spin axis. Quite often, since the attitude adjustments often took place after apogee, the data in the first half of an attitude adjustment orbit served this purpose. The second calculation was performed over the two hours or so immediately following the adjustment and resulted in the value of  $D_z$ , the spin axis offset, which can be related to the required quantity  $\Delta_3$  in Eq(39). In the following description of these calculations, we will refer to quantities such as  $r_{xy}$ , instead of  $r_{xy1}$  and  $r_{xyh}$ , since the calculation is identical in either gain state.

The first step in the calculation is to use previously determined values for the alignments  $\theta_i$  and  $\phi_{ij}$ , and the gain ratios  $r_{xy}$  and  $r_{xz}$  to cast the signals into the spacecraft frame. The coordinate frame employed here is equivalent to that of Eq(12). Conversion is done by multiplication of  $s_y$  by  $r_{xy}$  and of  $s_z$  by  $r_{xz}$ , then multiplying the triad by the inverse of Eq(12).

$$\begin{bmatrix} \Sigma_x \\ \Sigma_y \\ \Sigma_z \end{bmatrix} = A^{-1} \begin{bmatrix} s_x \\ r_{xy}s_y \\ r_{xz}s_z \end{bmatrix} \quad (43)$$

Figure 12 shows what these signals look like for a typical orbit. The spin axis field (z) is not modulated, although it shows some interesting structure. Since the pseudo-sensors  $s_x$  and  $s_y$  are perpendicular to the spin axis and to each other, and since we multiplied  $s_y$  by the gain ratio, Eq(6) becomes

$$\Sigma_x = g_x b_{xy} \cos(\omega t + \phi_b) + D_x \quad \Sigma_y = g_x b_{xy} \sin(\omega t + \phi_b) + D_y \quad (44)$$

which is to say that the dc component of the signals is purely sensor offset. These are fit to a slightly different spin fit function

CRRES Spacecraft Frame Magnetic Fields --- Orbit 066

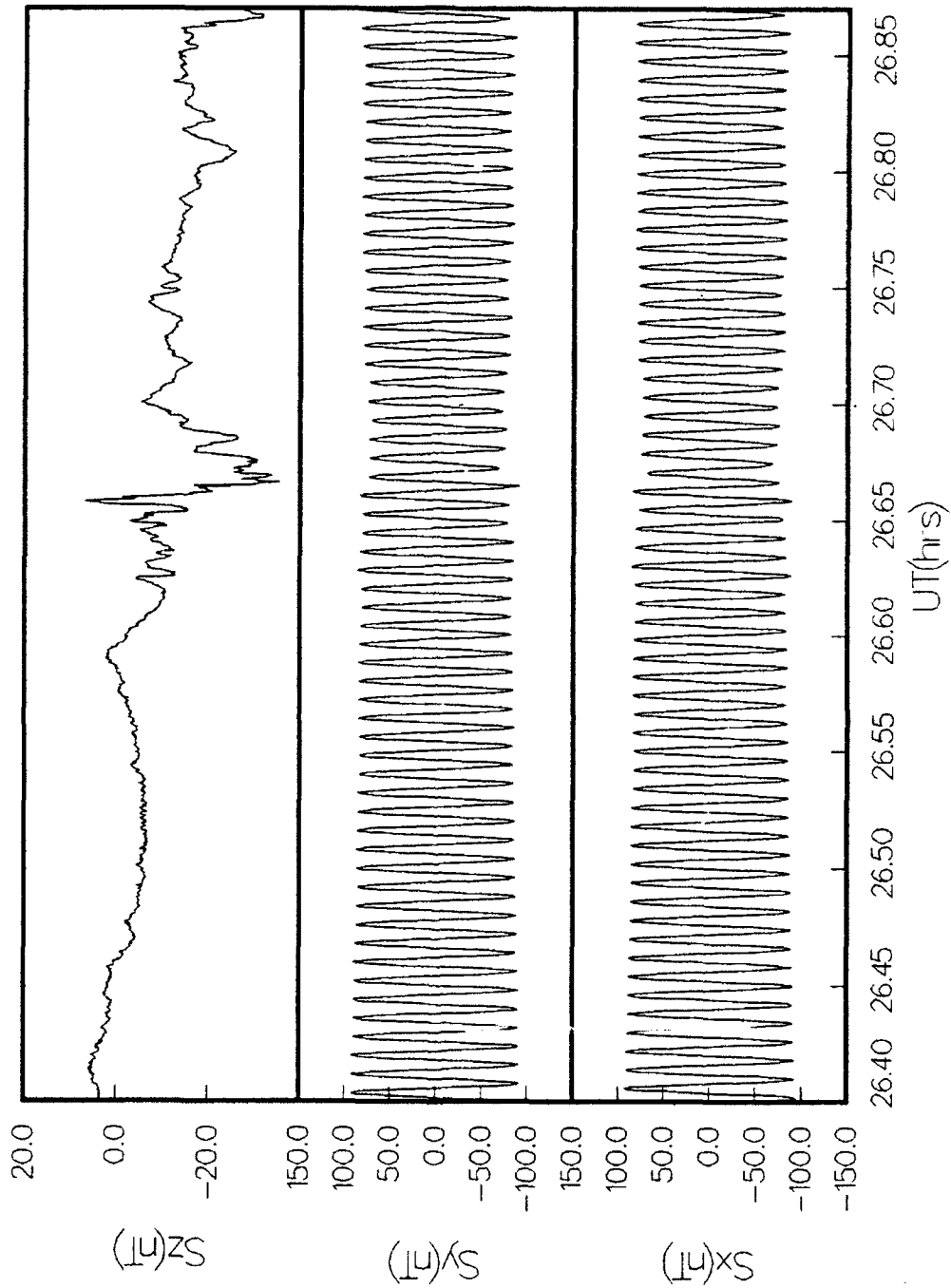


Figure 12. Magnetic field in the spacecraft frame.

$$s = \delta_0 + \alpha_1 \cos \omega t + \beta_1 \sin \omega t + \alpha_2 t \cos \omega t + \beta_2 t \sin \omega t + \dots \quad (45)$$

which differs from Eq(10) in that there is no variation allowed in the dc portions, since this is purely sensor offset. The results of these are averaged over selected periods to produce  $D_x$  and  $D_y$  values for the next step.

When the satellite nutates, the spin axis (z) moves through an angle of as much as  $10^\circ$  with respect to the background field. The frequency of this motion is about 4 rpm, or twice the spin rate, so that the background field remains relatively constant during a few cycles when the field is quiet. Figure 13 shows the beginning of nutation after an attitude adjustment. Two different methods were employed in the calculation of bias. One, developed by *Aerospace, Inc.* [1986], was intended to be used during precessions and gave higher noise levels than the second method, developed by us, when applied to nutation situations. We include it here for completeness, although the results were used only for comparison.

The offsets  $D_x$  and  $D_y$  are first subtracted from the pseudo-sensor signals

$$\sigma_x = \Sigma_x - D_x \quad \sigma_y = \Sigma_y - D_y \quad (46)$$

Then, two signals representing spin axis positions but the same external field are compared. The squares of the magnitudes are equated and the expression is solved for  $D_z$ , giving

$$D_z = \frac{\sigma_{x1}^2 + \sigma_{y1}^2 + \Sigma_{z1}^2 - (\sigma_{x2}^2 + \sigma_{y2}^2 + \Sigma_{z2}^2)}{2(\Sigma_{z1} - \Sigma_{z2})} \quad (47)$$

This method suffers from noise in that it uses only two points in each calculation. It also requires quite a bit of motion to change the values of  $\Sigma_z$  appreciably. Because of the high noise level, we used it mostly as a check on our own method, described next. We found that, averaged over the hour or so after an attitude adjustment, the methods agreed to about one count in most cases.

The second method assumes that the variation of the magnitude of the external field can be represented by a polynomial in time.

$$|b_{ext}| = \{\sigma_x + \sigma_y + (\Sigma_z - D_z)\}(t) = a_0 + a_1 t + a_2 t^2 + \dots \quad (48)$$

Assuming different values for  $D_z$  in Eq(48), we perform the fit and calculate the residual

$$R(D_z) = \sum_i ([\sigma_{xi}^2 + \sigma_{yi}^2 + (\Sigma_{zi} - D_z)^2]^{1/2} - [a_0 + a_1 t_i + a_2 t_i^2 + \dots])^2 \quad (49)$$

Figure 14 shows one of these residuals as a function of  $D_z$ . By finding the minimum of this residual, we can find the best estimate for  $D_z$ . Figure 15 shows a series of these calculations,

CRRES Spacecraft Frame Magnetic Fields --- Orbit 1020

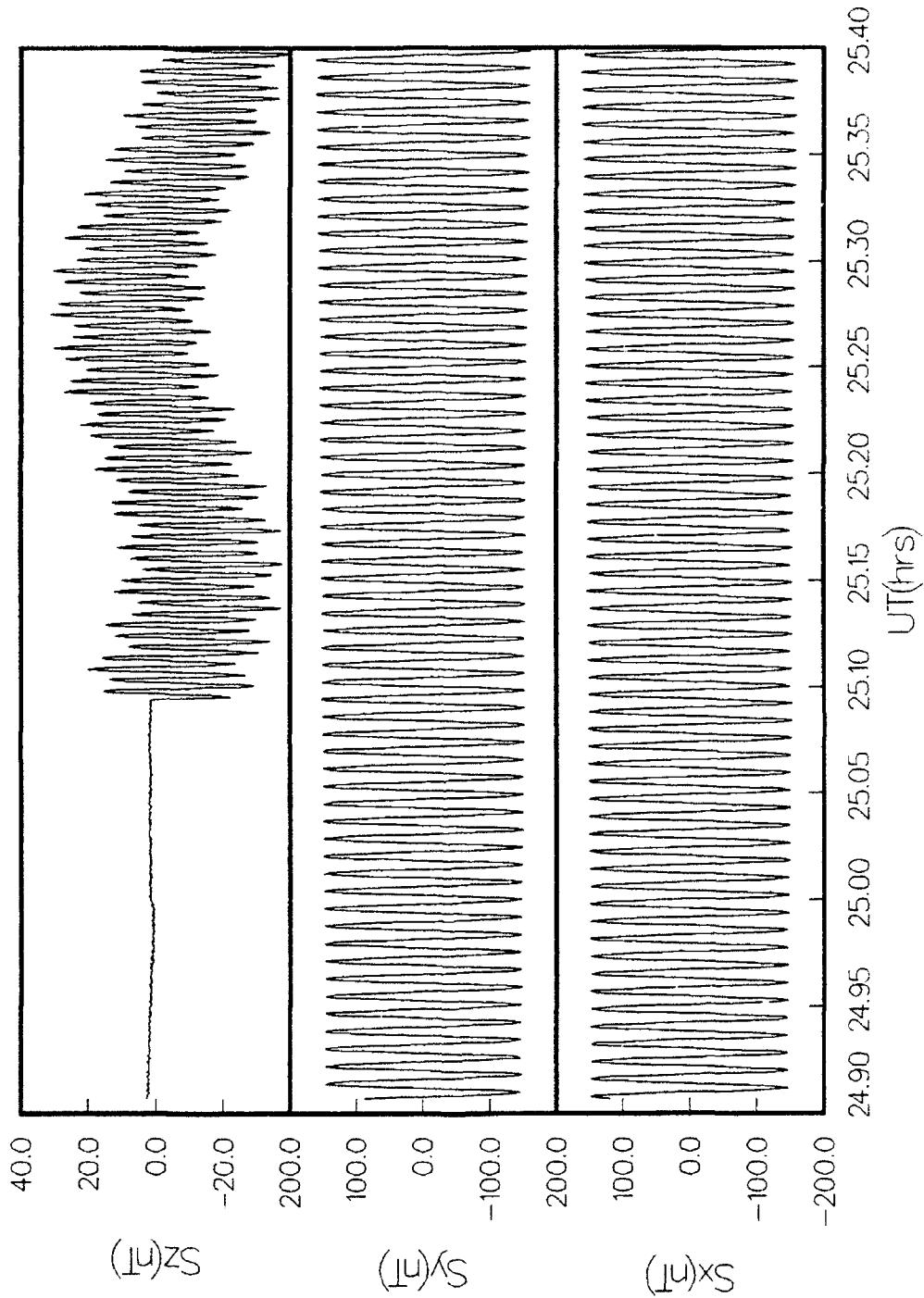


Figure 13. The beginning of nutation following an attitude adjustment.

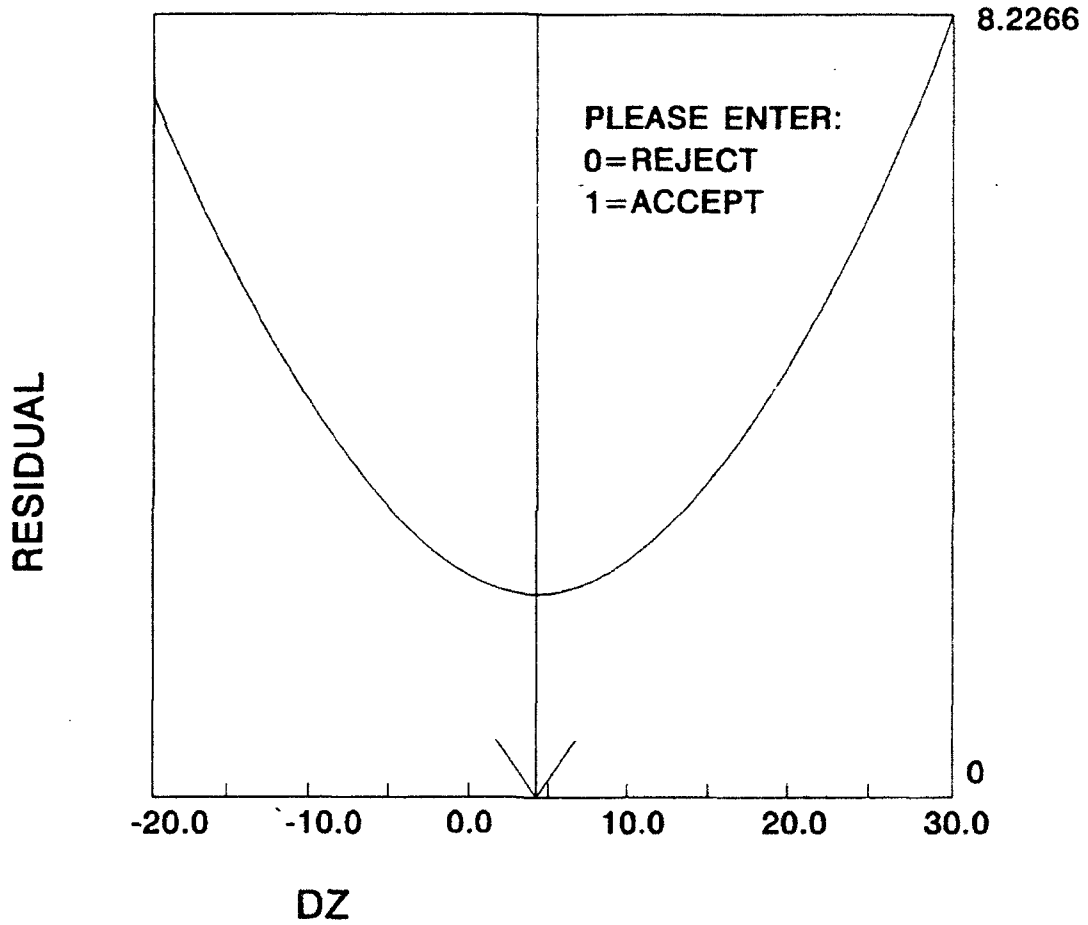


Figure 14. Magnetic field magnitude minus model as a function of  $D_z$ .

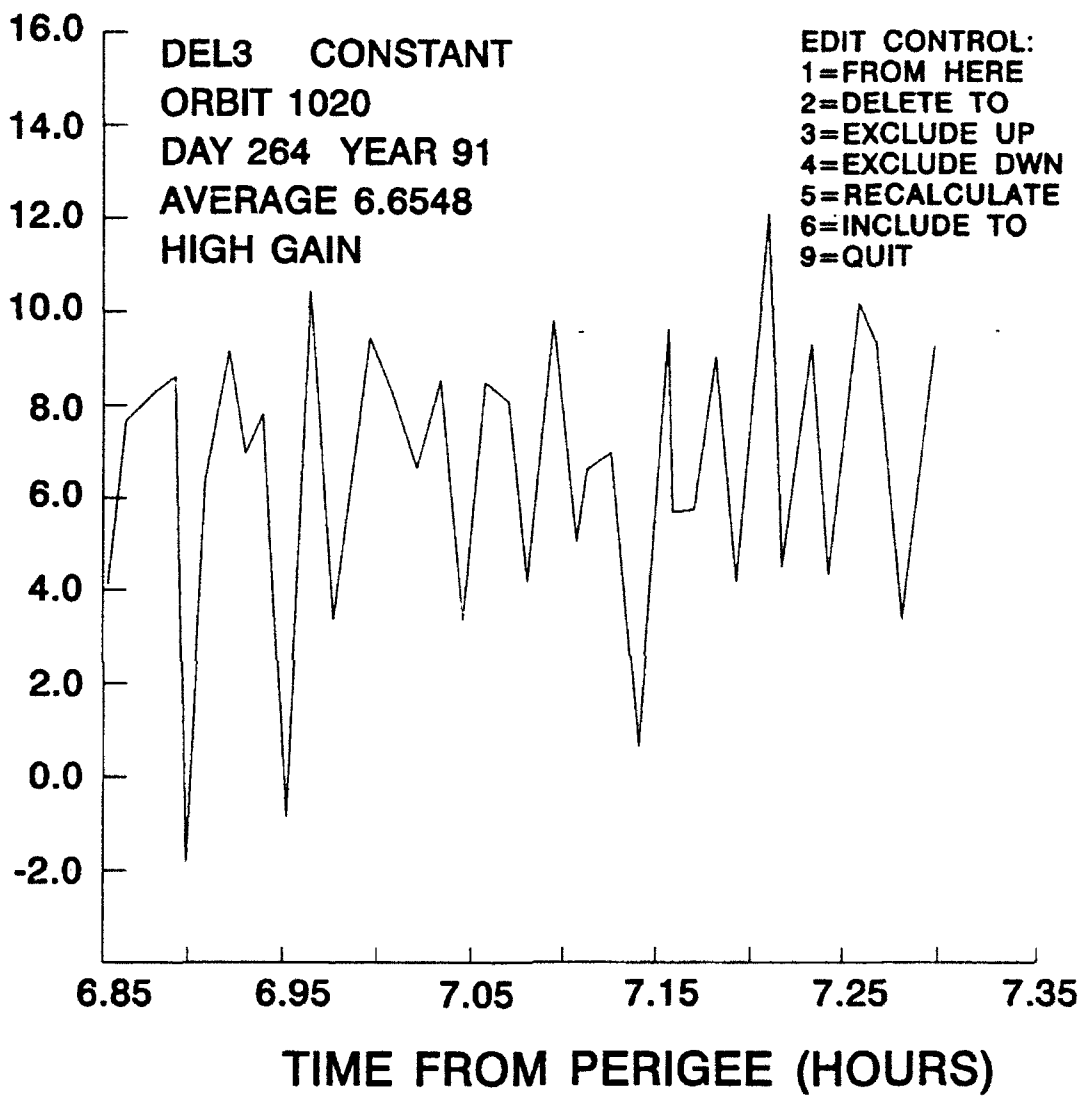


Figure 15. A series of  $D_z$  calculations following an attitude adjust.

over the course of about one-half hour following an attitude adjustment. Although there is considerable noise even in this method, the average can clearly be estimated at around 6 counts.

In order to arrive at a value of  $\Delta_3$  from these measurements, we must relate  $\Delta_3$  to the  $D_i$ 's measured. With the known alignments, we can write

$$d = A^{-1} D \quad (50)$$

which gives us the individual sensor offsets which are then substituted into Eq(39). Doing this shows that  $\Delta_3 \approx D_z$  for all practical purposes.  $\Delta_3$  is *not* the offset of the y-sensor, due to the large contribution from the x-sensor offset, which itself is large in magnitude.

Throughout most of the mission, the measured value of  $\Delta_3$  remained much higher than in the present example. Upto Orbit 850, the value stayed within a couple counts of 13. At that time, the offset of the x-sensor began to change, falling from about 90 counts to about 55 counts by orbit 920 or so. Since  $\Delta_3$  contains a contribution from  $d_x$ , its value also declined.

We had an opportunity to check on this calculation during the large Barium chemical releases G8 and G10, in which completely diamagnetic cavities were formed. When the cavity surrounded the satellite, the sensor offsets could be obtained directly from the sensor readings. For the two releases, the offsets of the sensors were 90 counts for x, 12 counts for y and 13 counts for z. This works out to give a value of 10.5 counts for  $\Delta_3$ . During the release, however, the power amplifier was on. We know from Figure 11 that  $d_x$  drops by about 2 counts when the amplifier is turned on. Examination of  $b_z$  at this time shows a total change of about 1 nT or 2 counts total. Adding this to the result gives reasonable agreement with the  $\Delta_3$  value measured in the bias calculation.

## 5.2. Calculation of X-sensor Phase

Throughout the data processing, the magnetometer data was used to check the accuracy of the attitude solution and of the attitude model produced. The methods for attitude determination for CRRES are described in another document [McNeil, 1991]. The attitude quality control check was carried out after attitude modeling by calculating the angular difference between the Earth Centered Inertial frame magnetic field as determined from the reduced magnetometer data and the IGRF85 model field, included in the ephemeris data. The angular deviation thus represented the total error from calibration, attitude calculation and inherent model field inaccuracies. Because of the high perigee of the satellite, the deviation over most of the orbit was high due to contributions from the external field, which can deviate from the instantaneous field by as much as  $10^\circ$ , even in quiet periods. However, the data in the first hour or so pre- and post-perigee, where internal magnetic sources dominate, served as a good indication of overall accuracy.

We noticed quite early on that there appeared at perigee an approximately  $3^\circ$  discrepancy between measured and model field. Additionally, we discovered that this discrepancy was for

the most part perpendicular to the spin axis. We also noticed that subtraction of about 200 ms from the assumed time of the reading led to consistently better results. After a rather intensive search for possible timing errors, in either the magnetic field measurements or the attitude, we concluded that the phase of the magnetometer was probably somewhat in error. This seemed reasonable since videotape of ground tests of the boom revealed that the magnetometer mounting rocked somewhat during deployment and since locking never took place.

In order to determine an optimum value for the phase  $\phi_x$ , a survey was carried out of one hundred orbits. For the first half-hour of each one, the function

$$F(\phi_x) \equiv \sum \cos^{-1} \left[ \frac{b_m \cdot b_e}{|b_m| |b_e|} \right] \quad (51)$$

was minimized in steps of  $0.1^\circ$ . In Eq(51),  $b_m$  is the measured magnetic field after calibration and conversion to ECI coordinates and  $b_e$  is the model field. After rejection of orbits immediately following attitude adjustments and averaging, this yielded a value of  $177.4^\circ$ . For all orbits in this period not following attitude adjust orbits, using this value gave a rms average error of  $1^\circ$  or less within one hour of perigee. This error is probably due largely to errors in the attitude, which is accurate to only  $0.5^\circ$  in the spin axis at best, and probably by at least that much in the spin phase.

Further validation of this assumption came when data from early orbits were analyzed. Orbits prior to Orbit 55 were not routinely processed due to the high spin rate. It was found that for the early orbits, with spin rate  $> 10$  rpm, the chosen value of  $\phi_x$  did equally as well as in the low spin rate orbits. Had the error been the result of timing instead of phase, on the other hand, the high spin rate would cause a large angular deviation. At 10 rpm, for example, a 200 ms timing error gives more than a  $12^\circ$  error. For orbit 31, with  $\omega=9.6$  rpm, the chosen  $\phi_x$  value led to agreement of better than  $0.5^\circ$  at perigee.

### 5.3 Calculation of Absolute Gain

Just as the direction of a model field can be used to obtain the absolute phase of the magnetometer axes, the magnitude can be used to obtain absolute gain. If we subtract the offsets, then multiply the y-sensor signal by  $r_{xy}$  and the z by  $r_{xz}$  and divide by the magnitude of the model field,

$$g_x^{-1} = \left[ \frac{(s_x - d_x)^2 + r_{xy}(s_y - d_y)^2 + r_{xz}(s_z - d_z)^2}{b_e^2} \right]^{1/2} \quad (52)$$

with  $g_x$  in nT/count. We performed this calculation on several orbits initially, finding that the values obtained fluctuated around the ground measured value by a part-per-thousand or so.

Having thus confirmed the ground measurement on-orbit, we opted to use the ground measured value for all orbits.

## 6. Despinning and Data Products

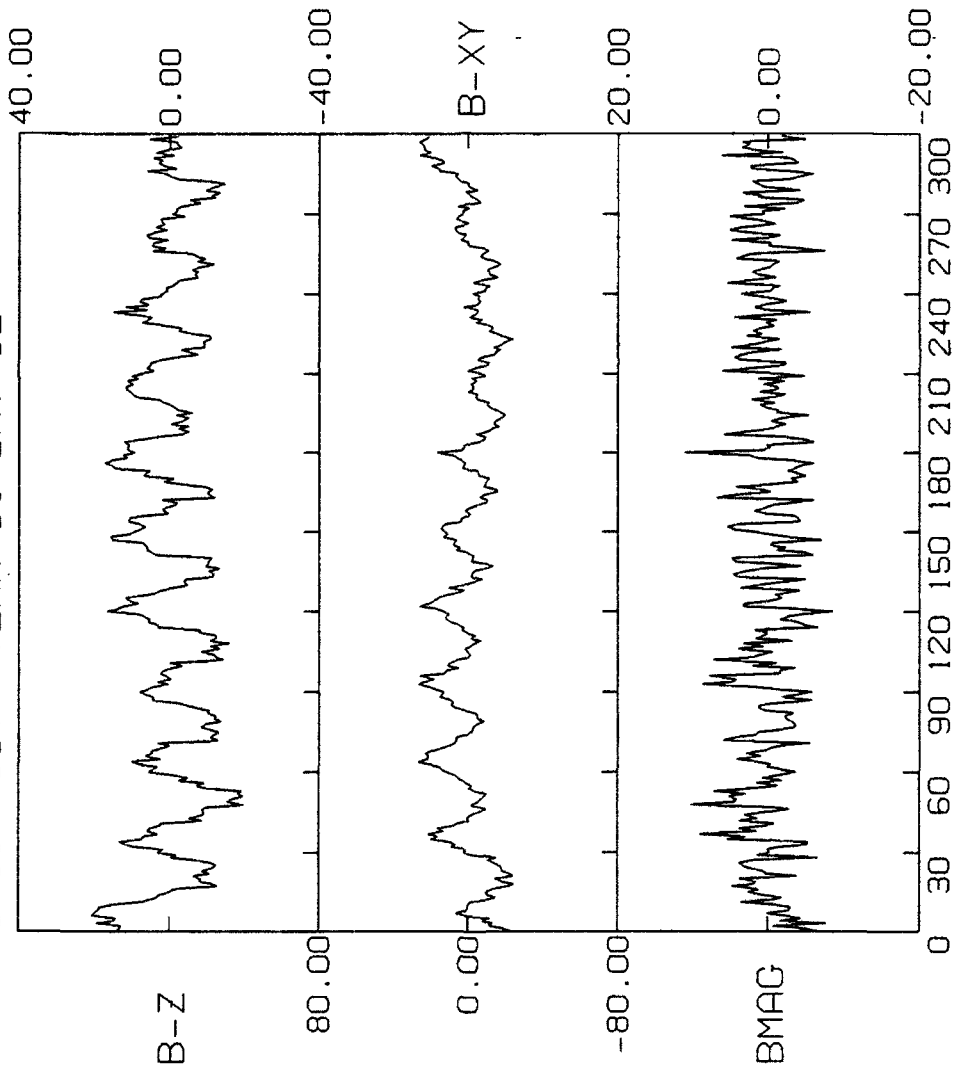
When the twelve quantities in Eq(1) have been calculated, the sensor equation is solved and the sensor signals are converted to the spacecraft frame in units of  $\mu T$ . Since the sensors are not quite orthogonal, the orthogonality angles are preserved by numerical inversion of the matrix instead of simple transposition. For the high gain data, offsets are calculated by 5-minute 'running averages' of the once-per-minute calculated offsets (Figure 11). This is done by first replacing each of the calculated offsets by the average of itself and the four surrounding values. Then a linear interpolation is performed to arrive at the offset for arbitrary times. We should note here that, for several orbits, complete calibration was not carried out due to vehicle events such as attitude adjustments or even due to intense geomagnetic activity. In these cases, calibration factors from other orbits were used and the orbit-averaged offsets replaced the 5-minute averages.

After conversion to the spacecraft frame, correction is made for the amplitude modulation of averaging by division of  $s_x$  and  $s_y$  by  $\chi_v$ . The correction for low gain samples originating from the fixed low gain channels is ignored, since it is small by comparison and since the conversion generally leads to the mixing of fixed low gain and variable gain samples. Along with the samples, a total number of points used in the creation of the three samples and a root mean squared standard deviation are calculated and passed along. The usual source of the sensor data is the one-second averaged data base, described in §4.2. The original 16-sample per second data is also subjected to the same process for selected periods when high frequency events of interest take place.

The soundness of the conversion of the sensor signals to the spacecraft frame is judged by two quality control plots. Figure 16 shows the first of these. This is a plot of the quantities  $b_z$ ,  $b_{xy} \equiv \sqrt{(b_x^2 + b_y^2)}$  and  $b_{tot}$ , all three with a cubic fit subtracted away. The utility of this fit is that miscalibration and misalignments will cause spin tone in the data. In the example shown in Figure 16, we see that there is a modulation in the  $b_z$  and the  $b_{xy}$  components, but not in  $b_{tot}$ . This could arise from misalignment but probably not from poor gain ratios or offsets. It could also be due to a slight motion of the vehicle, however. It is rather difficult to know for sure, since there is very long term motion following attitude adjustments, due to wire boom interaction. In any case, the modulation in Figure 16 amounts to less than  $0.1^\circ$ , and is actually quite good, being about one-half the resolution of the sensors. Resolution in the one-second data is enhanced through averaging.

Figure 17 shows another type of quality control plot, this time singling out the offsets in high gain. This plot was made by subtracting a 60-point running average from the quantity  $b_{tot}$ . Since gain errors would appear as modulation at a frequency of about twice per minute, this would appear as noise in Figure 17. The amplitude of the noise is thus a measure of the

CRRES MAGNETOMETER S/C DATA CHECK  
 ORBIT 587 YEAR 91 DAY 82



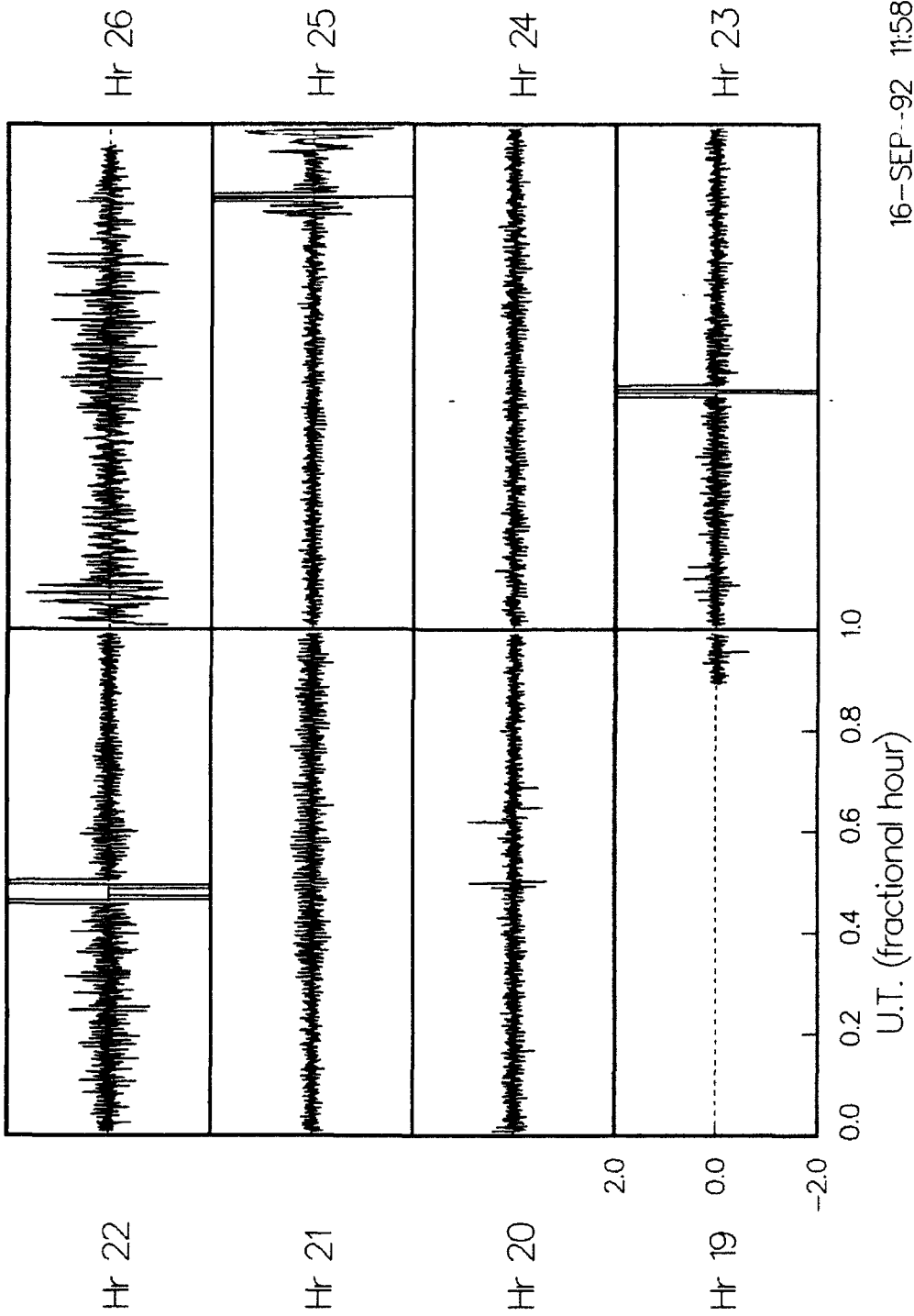
GXL -22.070  
 GYL -22.034  
 GYL6 0.4290  
 GZL -22.07329  
 GXH -0.42900  
 GYH -0.42690  
 GYH6 0.4290  
 GZH -0.42863  
 DXL 3.8  
 DYL 2.1  
 DYL6 0.0  
 DZL 2.2  
 DXH 92.5  
 DYH 12.1  
 DYH6 0.0  
 DZH 14.3  
 THX 14.21  
 THY -75.63  
 THZ 2.13  
 PHXY 9.31  
 PHXZ 90.45  
 FLAG 5.  
 300 LOW GAIN  
 0 HI GAIN  
 0 MIXED  
 0 X6 MODE

FIELDS - FIT (3)

SECONDS FROM 00:15:05 (REL) 18:44:05 (ABS) BMAX=17251

Figure 16. Quality control plot to examine spin tone in spacecraft coordinate fields.

Residual High Gain Spin Plane Modulation in nT  
Orbit 587 Day 82/91



16-SEP-92 11:58:48

Figure 17. Quality control plot of spin tone in high gain.

accuracy of the offsets. We can see that the spin tone is well below 0.5 nT throughout most of the orbit. This plot will also show considerable amplitude due to geomagnetic activity, which is probably the source of the amplitude in Hour 26. Had we used orbit averaged offsets, instead of the 5-minute averages of Figure 17, we would see a constant spin tone of about 1 nT, which is approximately half the residual spacecraft offset due to the power amplifier and/or due to cooling during eclipse.

Following conversion to spacecraft coordinates, the attitude model is used to transform the sensor signals, now in nT, to the Earth Centered Inertial coordinate frame [Bhavnani and Vancour, 1991]. The attitude is evaluated from model coefficients, as described in McNeil [1991], and results in the right ascension and declination of the spin axis,  $\alpha$  and  $\delta$ , and in a phase angle  $\phi$ . The spacecraft axes, in ECI coordinates, are given by the matrix  $R$

$$R = \begin{bmatrix} \sin\delta\cos\alpha\cos\phi - \sin\alpha\sin\phi & \sin\delta\sin\alpha\cos\phi + \cos\alpha\sin\phi & -\cos\delta\cos\phi \\ -\sin\delta\cos\alpha\sin\phi - \sin\alpha\cos\phi & -\sin\delta\sin\alpha\sin\phi + \cos\alpha\cos\phi & \cos\delta\sin\phi \\ \cos\delta\cos\alpha & \cos\delta\sin\alpha & \sin\delta \end{bmatrix} \quad (53)$$

and the magnetic field is obtained in ECI coordinates by multiplication by  $R^{-1}$ .

As with the spacecraft frame data, the ECI frame data is checked routinely with a quality control plot. One such is shown in Figure 18. The left panel shows the angle between measured and model field. The values near perigee give a good indication of the accuracy, since the model field is quite good near the earth. The right panel shows the magnitude of the measured field divided by the magnitude of the model. A second type of ECI quality control plot is shown in Figure 19. There, the three components of the model field are subtracted from the measured field converted to ECI. Since conversion requires despining with the attitude model, modulation at the spin frequency would be evidence of improper processing.

### 6.1 The Two-Second Data Base

The working data base for science in the magnetometer experiment is a two-second data base produced from the results of the ECI conversion above. The two-second samples are formed from three separate one-second averages according to

$$b_i = \frac{1}{4}(b_{i-1} + 2b_i + b_{i+1}) \quad (54)$$

to minimize aliasing. They are packed into 32-bit positive integer format to allow for easy transfer between mainframes. The format of the two-second data is given in the appendix.

Orbit 1010 Day 260/91 Start UT 11.283 (hrs)

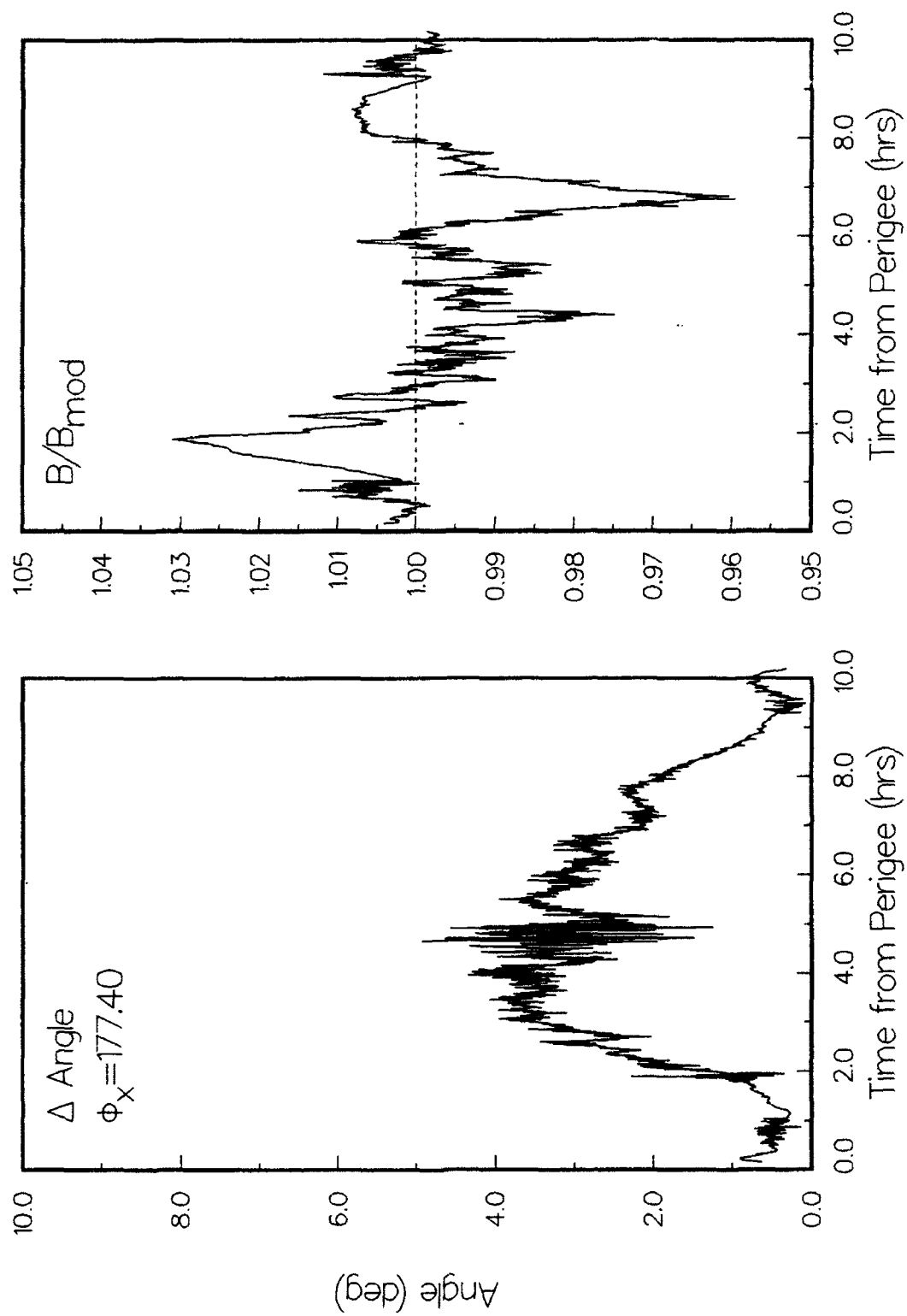


Figure 18. Quality control plot of model field angle and magnitude deviation from measured field.

ECI MAGNETIC FIELD COMPONENTS

ORBIT 587 YEAR 91 DAY 82

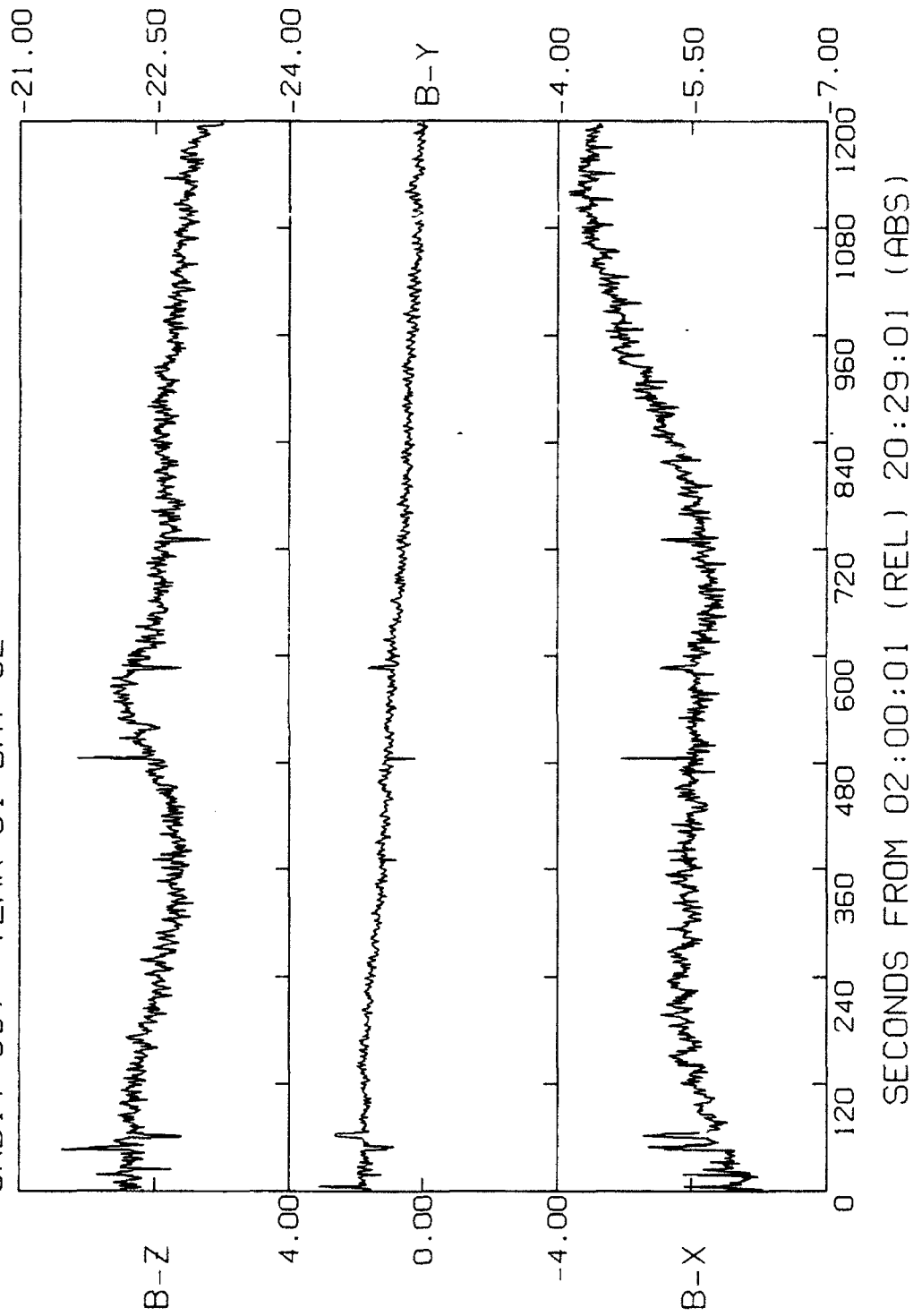


Figure 19. Quality control plot of measured minus model field.

## 6.2 The VDH Summary Plot

From the one-second averaged data, a plot is produced in the VDH coordinate system. In this system, the z-axis is collinear with the earth's dipole axis and the spacecraft position vector lies in the xz-plane. The origin chosen is the center of the earth. The ECI one-second data is first averaged in sets of 60 points then converted to VDH and displayed, along with  $b_{\text{tot}}$  and the IGRF85 + Olsen-Pfitzer77 quiet external field model. The components have this model subtracted. A typical example is shown in Figure 20. Several relevant quantities are listed beneath the x-axis of the plot as well. In Figure 20 we see some Pc class activity perpendicular to the magnetic field ( $z_{\text{VDH}}$ ) between 15 and 16 hours UT.

## 6.3 The Ultra-Low Frequency Spectrogram

The one-second data is also used to produce a spectrogram in the frequency range from zero to about 100 mHz. One such is shown in Figure 21. To perform these plots, the ECI magnetic field components are first averaged over 5-minute intervals. A running window of 128 five-minute averages are used to increase the resolution, the window moving by 32 five-minute samples for each spectrum. To cut down on background power, a fifth order polynomial fit is subtracted from the components. The power spectrum of each component is taken, then the squared power from each is summed and multiplied by the frequency to give units of  $nT^2$ . We can see that the waves in Figure 20 appear in Figure 21 as well. However, higher frequency waves would be effectively averaged out in the VDH survey plot. In fact, we can see a strong wave shortly after 13 hours UT that does not appear in Figure 20.

## 6.4 The Ion Cyclotron Spectrogram

After producing the low frequency plots from averaged data, processing returns to the 16-sample/second data to produce the ion cyclotron spectrogram, spanning frequencies up to 8 Hz. In performing these transforms, the data is converted to the spacecraft frame but, to cut down the processing time, is not converted to the ECI coordinate system. Instead, transforms are done on  $b_z$  and  $b_{xy}$ . After subtracting a sixth order fit, the power from these components is squared and summed and, again, multiplied by the frequency to obtain  $nT^2$ . One spectrogram is shown in Figure 22. The black line plotted is the gyrofrequency of a proton, deduced from the measured magnetic field. We see in Figure 22 an event at 17:20 UT at the proton gyrofrequency and its first harmonic. These plots were crucial to spotting the ion cyclotron events during the mission, which were few and far between.

## 6.5 16-Sample/second Processing

The full high time resolution data, as 16-samples/second, was not processed in every case except for the creation of the ICW spectrograms described above. Instead, the spectrograms were examined and periods of interest were selected in which high frequency events took place. To these data were applied the same calibration factors and despinning procedures described above, except that no data was edited in any way. It was thought best to avoid any possibility

CRRES VDH Magnetic Fields Orbit 1010 260/91 Sep 17

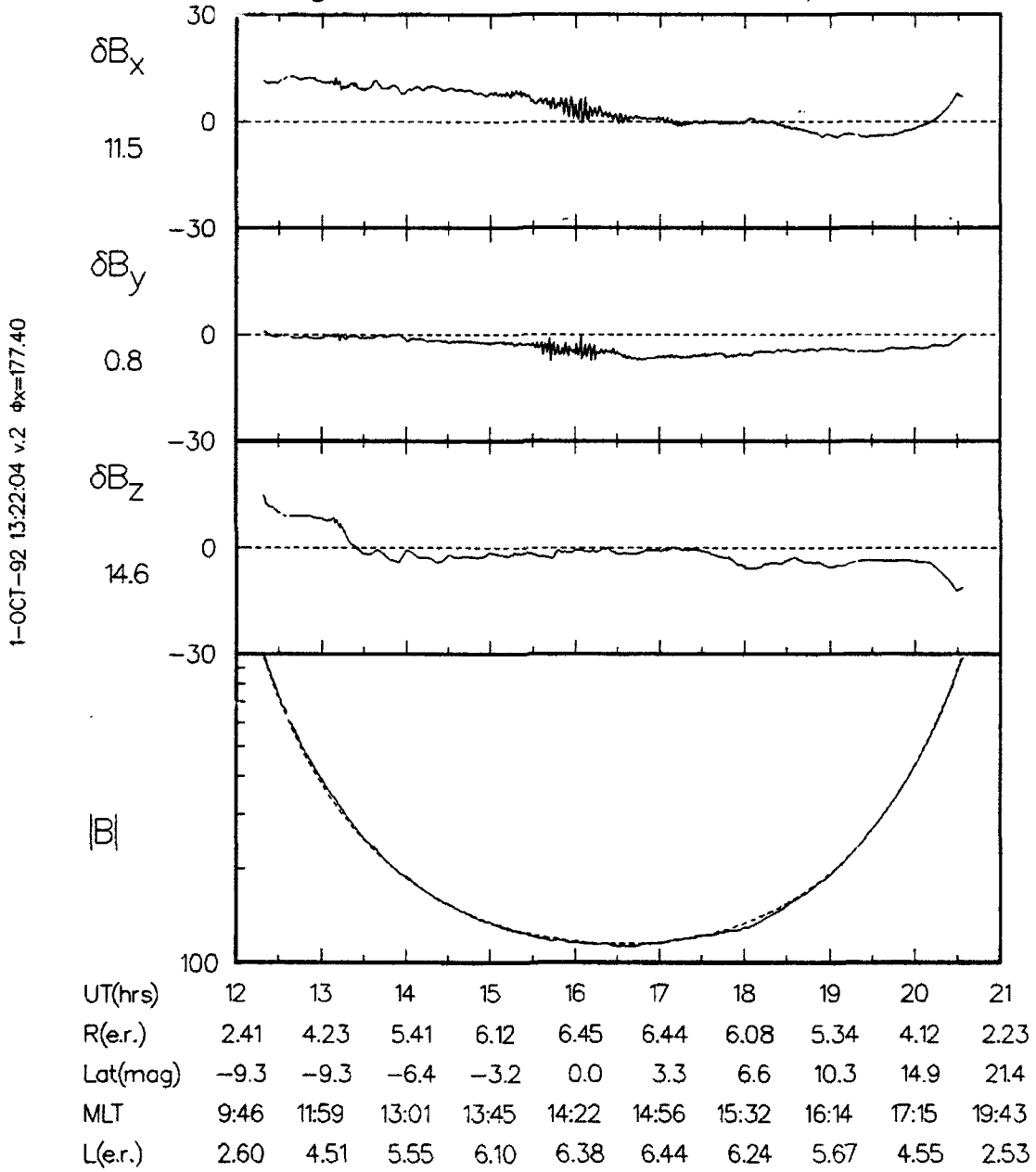


Figure 20. VDH survey plot.

1992-07-21 12:00:14

CRRES ULF Wave Spectrogram Orbit 1010 260/91 Sep 17

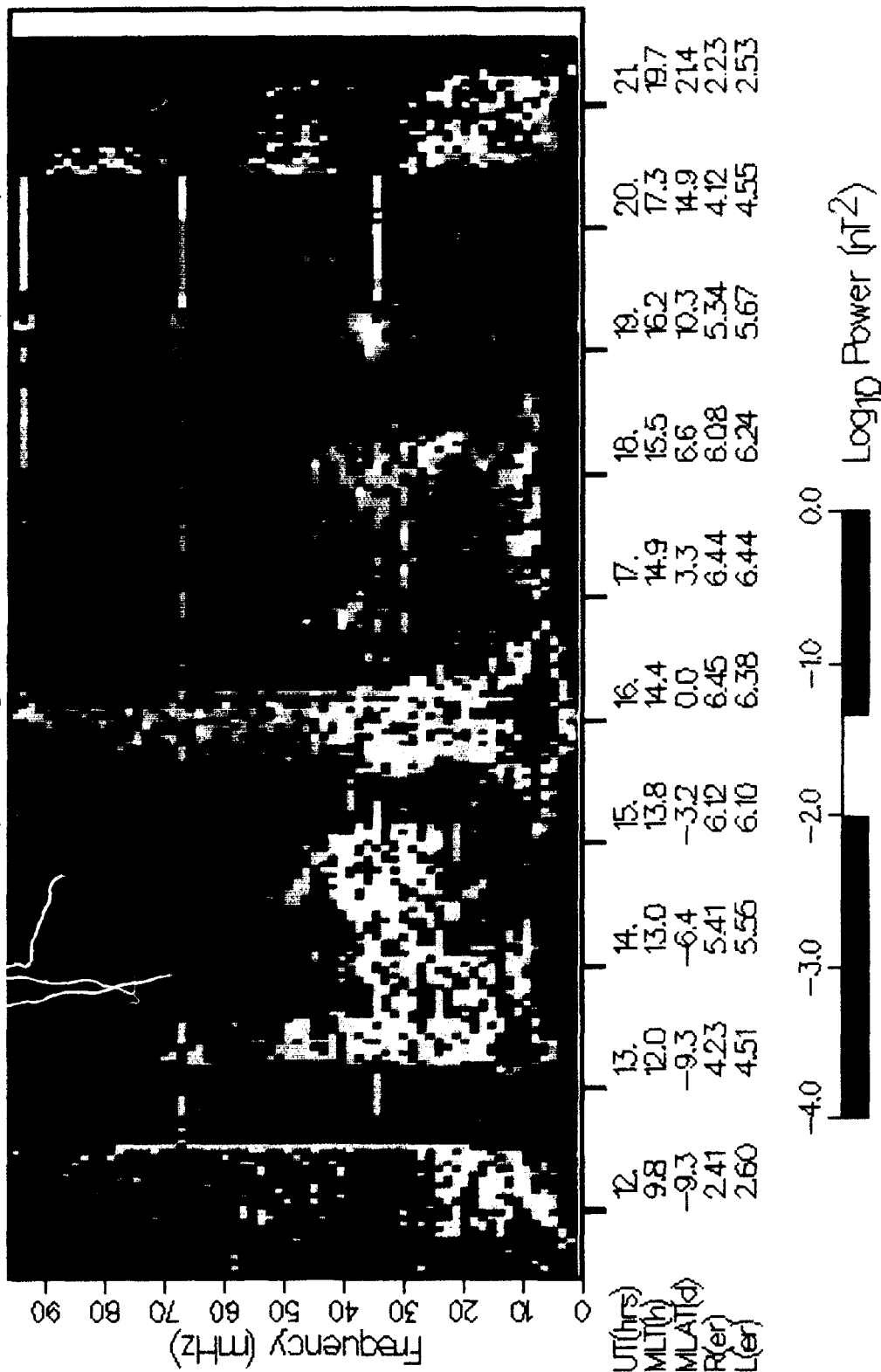


Figure 21. Ultra-Low Frequency Spectrogram.

9-JUN-93 14:07:37

CRRES ICW Wave Spectrogram Orbit 1029 268/91 Sep 25

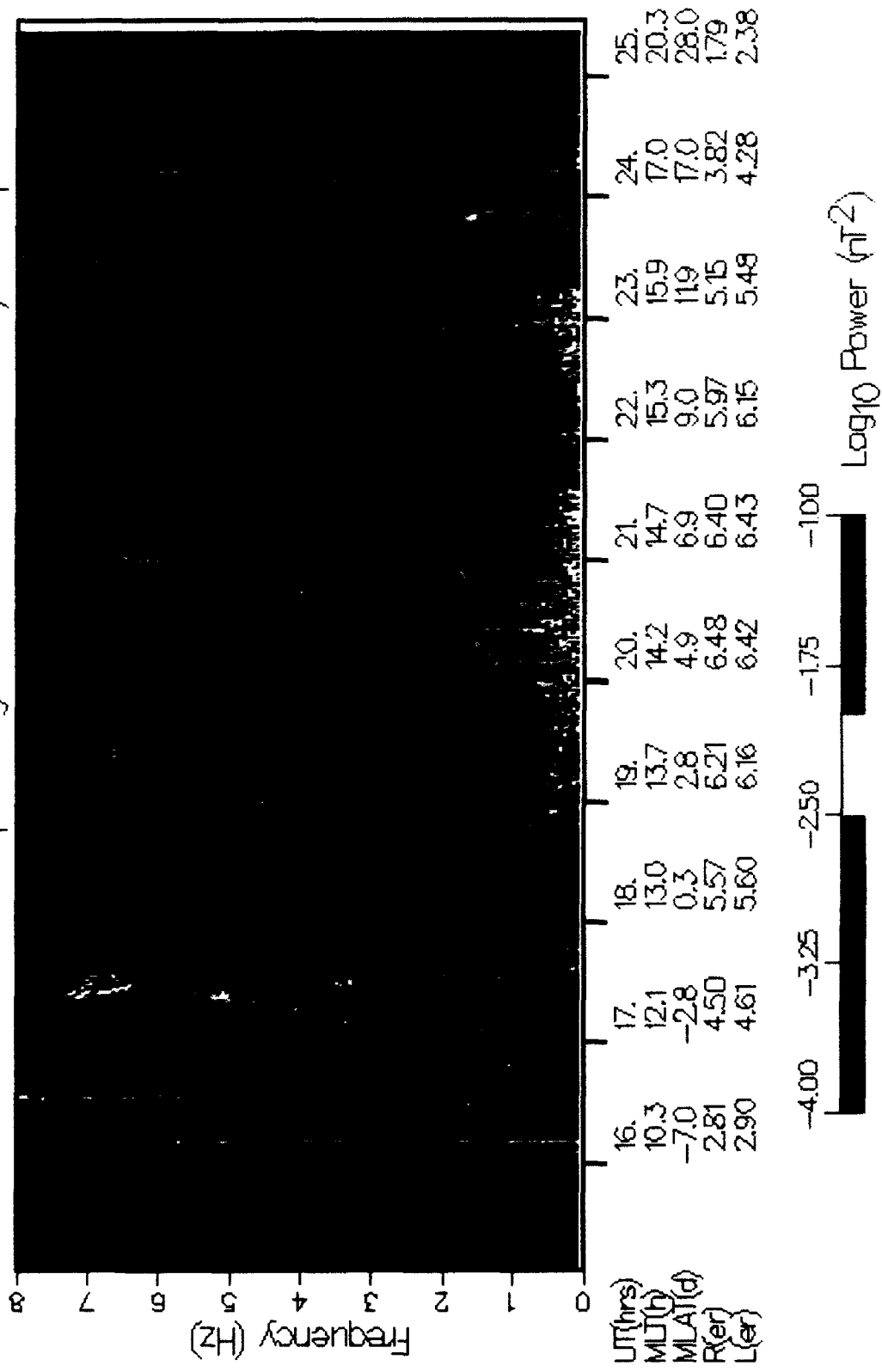


Figure 22. Ion Cyclotron Wave Spectrogram.

of discarding good data in this processing. The data was packed in much the same way as the two-second data base and shipped to mass storage for archival and use. The file format is given in an appendix.

## 6.6 Quick Look Plots

Early on in the processing, we realized that processing of the data would lag acquisition by at least a month or two. In order to keep more up to date on the performance of the instrument, we began to produce plots much like Figure 20 each time new data was acquired. These were made with calibration factors from previous orbits. These plots proved valuable in spotting periods of interesting geomagnetic activity and were responsible for the early detection of several instrumental problems.

## 7. Conclusion

The techniques used in the CRRES fluxgate magnetometer processing were the result of a relatively lengthy and elaborate effort in simulation and analysis. They are, we believe, somewhat novel and have proven to be quite effective. The account of the processing given here should serve as an historical record of the methods, important in understanding the data produces and perhaps even for applications to other missions.

## References

Aerospace, Corp., *private communication*.

Bhavnani, K.H. and R.P. Vancour, "Coordinate Systems for Space and Geophysical Application", PL-TR-91-2296, Phillips Laboratory, Hanscom AFB, 11 December 1991, ADA247550.

Hornbeck, R.W., "Numerical Methods", Quantum Publishers, Inc., New York, 1975.

McNeil, W., "On-orbit Fluxgate Magnetometer Calibration System Product Specification and Test Results for CRRES", Radex, Inc., Carlisle, Mass. 29 June 1987.

McNeil, W. and H.J. Singer, "Fluxgate Magnetometer Analysis and Simulation Software for the Combined Release and Radiation Effects Satellite (CRRES)", AFGL-TR-86-0222, Air Force Geophysics Laboratory, Hanscom AFB, Mass., 1 October 1986, ADA176353.

McNeil, W. and R.E. McInerney, *private communication*, 27 May 1988.

McNeil, W., "Calculation and Modeling of the Attitude for the Combined Release and Radiation Effects Satellite", PL-TR-91-2239, Phillips Laboratory, Hanscom AFB, Mass., 26 September 1991, ADA243950.

Press, W.H., B.P. Flannery, S.A. Teukolsky and W.T. Vetterling, "Numerical Recipes", Cambridge University Press, Cambridge, 1986.

Singer, H.J., W.P. Sullivan, P. Anderson, F. Mozer, P. Harvy, J. Wygant and W. McNeil, "The Fluxgate Magnetometer Instrument on the Combined Release and Radiation Effects Satellite", *J. Space. Roc.*, **29**, 599, 1992.

## Appendix A - File Formats

### The 16-sample/second Magnetic Field File

The following table shows the quantities contained on the 16-sample/second magnetic field file and the location in telemetry from which they were extracted.

Byte	Location <sup>1</sup>	Quantity
1-4	none	UT(ms) of SF 0
5	[223,2]	B1
6	[223,3]	B2
7	[223,11]	B31
8	[223,20]	B30
9	[223,21]	B13
10-15	[93,0]-[93,5]	BEXL,BEYL,BEYL,BEX,BEY,BEZ <sup>2</sup>
16	[189,10]	Mag. Elect. Temp.
17	[189,29]	Mag. Probe Temp.
18	[221,0]	28 V Current Mon.
19	[221,1]	5 V Current Mon.
20	[221,2]	Temp 1B Mon.
21	[221,3]	12 V Mon.
22	[221,4]	5 V Mon.
23	[221,5]	15 V Mon.
24	[221,6]	35 V Mon.
25-27	[169,5]-[169,7]	BXA0,BYA0,BZA0 <sup>3</sup>
28-30	[169,13]-[169,15]	BXA1,BYA1,BZA1
31-33	[169,21]-[169,23]	BXA2,BYA2,BZA2
34-36	[169,29]-[169,31]	BXA3,BYA3,BZA3
37-39	[251,29]-[251,31]	BXAL,BYAL,BZAL
40	[221,2]	Temp. 1B Mon.
41	[157,0]	CMPT#2 BLKHD#1 Temp.
42	[157,20]	CMPT#2 Rim PNL Temp.
43	[238,5]	Search Coil Temp #1
44	[238,13]	Search Coil Temp #2

<sup>1</sup> Location refers to the place in the telemetry stream from which the data was extracted, *i.e.*, [byte number, subframe].

<sup>2</sup> Engineering Magnetometer Readings

<sup>3</sup> Fluxgate analog signals.

45	[238,21]	Search Coil Temp #3
46	[238,29]	Search Coil Temp #4
47-48	[62,1]-[63,1]	Sun Crossing Time 1
49-50	[62,17]-[63,17]	Sun Crossing Time 2
51-52	[62,2]-[63,2]	Mag. Zero Time 1
53-54	[62,18]-[63,18]	Mag. Zero Time 2
55-56	[62,13]-[63,13]	Raw Spin Period
57-60	[223,0],[125,0]-[127,0]	VTCW of SF 0
61	[31,0]	SF 0 frame counter
62-73	[11,0],[14,0],[15,0] [43,0],[46,0],[47,0] [75,0],[78,0],[79,0] [107,0],[110,0],[111,0]	DSC1,MAG0,MAG1 <sup>4</sup> MAG2,MAG3,MAG4 MAG5,MAG6,MAG7 MAG8,MAG9,MAG10
74	[223,0]	B0 <sup>5</sup>
75	[31,1]	SF 1 frame counter
76-87	[11,1],[14,1],[15,1] [43,1],[46,1],[47,1] [75,1],[78,1],[79,1] [107,1],[110,1],[111,1]	EXP,MAG11,MAG12 MAG13,MAG14,MAG15 MAG16,MAG17,MAG18 MAG19,MAG20,MAG21
88	[223,1]	B1
89	[31,2]	SF 2 frame counter
90-101	[11,2],[14,2],[15,2] [43,2],[46,2],[47,2] [75,2],[78,2],[79,2] [107,2],[110,2],[111,2]	DSC2,MAG22,MAG23 MAG24,MAG25,MAG26 MAG27,MAG28,MAG29 MAG30,MAG31,MAG32
102	[223,2]	B2
103	[31,3]	SF 3 frame counter
104-115	[11,3],[14,3],[15,3] [43,3],[46,3],[47,3] [75,3],[78,3],[79,3] [107,3],[110,3],[111,3]	EXP,MAG33,MAG34 MAG35,MAG36,MAG37 MAG38,MAG39,MAG40 MAG41,MAG42,MAG43
116	[223,3]	B3

repeat 61-116 for 7 more "half-second" intervals

repeat 1-508 for 15 more master frames

8129-8160 "1"s filled

---

<sup>4</sup> See following appendix for format of magnetometer data.

<sup>5</sup> All bi-level values are included in [223,0] through [223,31] for each 4.096 second sample interval.

## Magnetometer Data Telemetry Format

The following table shows the locations of the 12-bit magnetometer readings within the 8-bit MAG words indicated in the preceding table.

```
00A 00B 01A 01B 02A 02B 03A 03B 04A 04B 05A 05B 06A 06B
**BX0L***** **BY0L***** **BZ0L***** *MD **BX0***** ***

07A 07B 08A 08B 09A 09B 10A 10B 11A 11B 12A 12B 13A 13B
BY0**** **BZ0***** **BZ1***** **BY1***** **BZ1*****

14A 14B 15A 15B 16A 16B 17A 17B 18A 18B 19A 19B 20A 20B
**BX2***** **BY2***** **BZ2***** **BX3***** **BY3**

21A 21B 22A 22B 23A 23B 24A 24B 25A 25B 26A 26B 27A 27B
*** **BZ3***** **BX4***** **BY4***** **BZ4***** ***

28A 28B 29A 28B 30A 30B 31A 31B 32A 32B 33A 33B 34A 34B
BX5**** **BY5***** **BZ5***** **BX6***** **BY6*****

35A 35B 36A 36B 37A 37B 38A 38B 39A 39B 40A 40B 41A 41B
**BZ6***** **BX7***** **BY7***** **BZ7***** **GX***

42A 42B 43A 43B
**GY*** **GZ***
```

---

nnA represents the left most four bits of MAGnn.

nnB represents the right most four bits of MAGnn.

Gi is the gain for the i'th sensor signals for the eight samples.

MD is a mode indicator 1 for x6 and 0 for x1. Although x6 mode was never used, this indicator did erroneously come on in certain periods.

## The Two-second Product Data Base

The product 2-second resolution ECI frame magnetic field file consists of byte-reversed integer data items, a header plus a series of one-minute data records. Each of the 32-bit quantities are described below. Conversion factors are used to recover the floating point values as indicated.

### 1: Header (Ephemeris and Calibration Information)

item	quantity	format
1	CRRES Vehicle I.D.	"CRES"
2	Orbit Number	integer
3	Modified Julian Date	integer
4	Year	integer
5	Day of Year	integer
6	UT at Start of Data	integer(ms)
7	UT at End of Data	integer(ms)
8	UT of first Ascending Node	integer(ms)
9	UT of first Perigee	integer(ms)
10	Data Rate	.001N ms
11	Date of Creation	"yymmdd"
12	Time of Creation	"hhmmss"
13	X-sensor low gain factor	1(-6)N - 1000
14	Y-sensor low gain factor	"
15	Z-sensor low gain factor	"
16	X-sensor high gain factor	"
17	Y-sensor high gain factor	"
18	Z-sensor high gain factor	"
19	X-sensor low gain offset	"
20	Y-sensor low gain offset	"
21	Z-sensor low gain offset	"

22	X-sensor high gain offset	"
23	Y-sensor high gain offset	"
24	Z-sensor high gain offset	"
25	x6 mode low gain factor	"
26	x6 mode high gain factor	"
27	x6 mode low gain offset	"
28	x6 mode high gain offset	"
29	X-sensor low gain P/A offset <sup>6</sup>	"
30	Y-sensor low gain P/A offset	"
31	Z-sensor low gain P/A offset	"
32	X-sensor high gain P/A offset	"
33	Y-sensor high gain P/A offset	"
34	Z-sensor high gain P/A offset	"
35	x6 mode low gain P/A offset	"
36	x6 mode high gain P/A offset	"
37	X-sensor elevation	"
38	Y-sensor elevation	"
39	Z-sensor elevation	"
40	X-to-y sensor relative azimuth	"
41	X-to-z sensor relative azimuth	"
42	X-sensor absolute azimuth	"
43	Offset average flag (0=orbit averaged)	"
44-128	Vacant (0 filled)	

---

<sup>6</sup> This was originally intended to be used for correction of the data during power amplifier operation, but ultimately was never used, since 5-minute averaged offsets were adopted instead.

2: Data records

word	bits	quantity	conversion factor
1	31-1	UT of first sample	integer ms
2	31-1	X-component of field 1 (nT)	.0001N - 45,000
3	31-1	Y-component of field 1	"
4	31-1	Z-component of field 1	"
5	31-1	X-component of field 2	"
		• • •	
91	31-1	Z-component of field 30	"
92	29-30 • 2-1	Range / Mode of field 1 • Range / Mode of field 15	(see note)
93	29-30 • 2-1	Range / Mode of field 16 • Range / Mode of field 30	
94	31-24 23-1	No. of points in average 1 Standard deviation of 1	integer .01N nT
		• • •	
123	31-24 23-1	No. of points in average 30 Standard deviation of 30	integer .01N nt
124- 128		Reserved (0 filled)	

Range/mode id is as follows: 0=low gain, 1=high gain, 2=x6, 3=mixed gains.

## The 16-sample/second Product Data Base

16-sample/second data is produced only during periods of interest. Like the two-second data, this is packed in 32-bit integers. The format is as follows.

### 1: Header

The header is identical to that of the two-second product data base.

### 2: Data Records

word	quantity	conversion factor
1	UT of first sample	integer ms
2	X-component of field 1 (nT)	.0001N - 45000
3	Y-component of field 1 (nT)	"
4	Z-component of field 1 (nT)	"
	• • •	
121	Z-component of field 40 (nT)	"
122	Gain state of fields 1-20	(see note)
123	Gain state of fields 21-40	(see note)
124-128	Reserved (0 filled)	

Gain states are indicated by right justified bits in these 32-bit words. Zero indicates that all samples are in low gain, ones-filled indicates high gain and other values indicate a mixture of gains in the sample set.

motion. Giant cells have been postulated in the deep convective zone but neither velocity measurements nor quiet-sun magnetic fields provide any evidence for their existence: we argue that supergranules may represent the largest energy-carrying scales throughout the convecting layer. The implications of these ideas are summarized in the concluding section.

## 2 THE UNDERLYING DYNAMICS

Granulation results from convective cells overshooting into levels that are stably stratified; immediately beneath the photosphere the convective contribution to energy transport is insignificant but by depths of 100–200 km almost all the energy is carried by convection. It is only at the scale of granulation that temperature variations and vertical velocities are strongly correlated, so granules must be responsible for energy transport at the top of the convective zone. Their observed scale extends from a minimum limit set by telescopic resolution (150 km) to the diameter ( $\sim 3$  Mm) of the largest exploders (Title *et al.* 1989; Spruit *et al.* 1990).

An exploder begins as a small bright feature, which then grows and develops a dark core at its centre. As the granule expands the rising central column is apparently slowed down by buoyancy braking until it is unable to supply enough energy to compensate for radiative losses. In some numerical models the density increases, owing to enhanced pressure and radiative cooling, until a downflow develops at the axis (Steffen, Ludwig & Krüss 1989; Spruit *et al.* 1990). After a lifetime of 10–20 min the exploder splits to form several fragments. This can be ascribed to purely hydrodynamic instabilities. A large granule resembles an axisymmetric vortex ring. In laboratory experiments vortex rings develop non-axisymmetric instabilities and numerical studies of Boussinesq convection show that axisymmetric cells become unstable to non-axisymmetric perturbations (Jones & Moore 1979).

The development of an exploding granule, with kinetic and dynamic pressures sufficient to sweep its neighbours aside, requires some external stimulus. Exploders occur preferentially near the centres of mesogranules, in regions of diverging flow (Title *et al.* 1989), and the measured velocity field of a mesogranule is apparently a combination of a systematic outflow and the cumulative effect of short-lived exploders distributed about its centre (Simon *et al.* 1991). Detailed observations from the Pic du Midi show that exploders emerge spasmodically near the centre of a mesogranule and expand as they move outwards (Muller *et al.* 1990, 1991). This process occurs repeatedly, at intervals of around 20 min, during the lifetime ( $\sim 3$  hr) of the mesogranule, indicating that there is a systematic mesogranular velocity. In addition, the time-averaged velocities of the exploders produce a contribution comparable to that of the mesogranular outflow (Simon *et al.* 1991). To explain this behaviour we assume that there is a weak mesogranular circulation in cells with radii of 3 Mm and similar depths. Superimposed on this is a shallow layer of granular convection with a depth of order 0.7 Mm. This configuration may become unstable to oscillatory modes, corresponding to hot and cold blobs of fluid circulating within the cell. Such an effect has been observed in the laboratory (e.g. Bergé &

Dubois 1979). Similar behaviour has also been studied in numerical experiments (Lennie *et al.* 1988), where secondary instabilities lead to periodic oscillations about a steadily convecting state. We postulate that the mesogranular circulation is dynamically coupled to the overlying granulation and that the combined system is liable to oscillatory instabilities. The temporarily enhanced circulation triggers the formation of exploding granules which then reinforce the original overturning motion. In a non-linear regime we would expect such oscillations to become aperiodic (*cf.* Lennie *et al.* 1988) and to develop into chaotic spatiotemporal behaviour. Thus we suggest a model in which mesogranules and granules are coupled by symbiotic oscillations, which generate bursts of exploders near the surface, so helping to maintain the mean flow. Note that the period of the oscillations ( $\sim 20$  min) is much shorter than the turnover time ( $\sim 3$  hr) for a mesogranule.

At the photosphere, mesogranules and supergranules have comparable velocities. Supergranules are easily recognized as the largest photospheric structures present in any region: they have lifetimes of a day or more, and there is a close correlation between their horizontal velocity structure and the magnetic network. Individual mesogranules drift towards the boundaries of supergranules, where they are destroyed (Muller *et al.* 1990, 1991). They can be detected by following the computed motion of passive test particles (corks) but do not affect the magnetic network to the same extent as long-lived supergranules. The vertical velocity, on the other hand, whether measured directly by the Doppler effect or inferred from the divergence of the horizontal motions, reflects the spatial scales of mesogranules, not supergranules (November 1989). Are the two phenomena dynamically coupled? A characteristic feature of non-linear convection is the presence of a thermal boundary layer immediately below the surface. If convection is sufficiently vigorous this boundary layer becomes unstable (Busse 1981). Laboratory experiments on Boussinesq convection provide examples of quasipermanent cellular patterns with ephemeral structures on a smaller scale (Busse 1981). More recently, precise experiments have shown how an unstable thermal boundary layer develops secondary structures at high Rayleigh numbers. Zocchi, Moses & Libchaber (1990) used capsules containing temperature-sensitive liquid crystals to visualize these structures. In their experiment, rising convective plumes excited waves within the upper boundary layer, and these waves developed into subsidiary plumes and spiral eddies as they crossed the layer. Thin subsidiary plumes eventually filled most of the convection cell. We suggest that the principal energy-carrying structures at depths greater than 1 Mm below the photosphere are supergranules, with an upper boundary layer in which the granules are embedded. Fluctuating velocities generate subsidiary structures which form a linear network of sinking material in this boundary layer. This network corresponds to the ephemeral mesogranules which are carried across the surface of the cell by the main supergranular flow.

Thus we are led to a description with two fundamental scales of subphotospheric convection, corresponding to granules and supergranules. Mesogranules develop within supergranules as subsidiary, parasitic features. Yet all these motions are dynamically linked – and it is through mesogranulation that supergranules are coupled to exploders.

### 3 DISCRETE SCALES IN THE CONVECTIVE ZONE

In the conventional picture of a stellar convection zone the scale of the energy-carrying eddies varies continuously with depth, with the mean value at any level related to an appropriate scaleheight. Thus the standard formulation of mixing-length theory introduces a characteristic scale proportional to the pressure scaleheight. This description can be expressed in a more appealing and sophisticated form, based on numerical simulations of convection in the Sun. Stein & Nordlund (1989) found that motion was dominated by rapidly sinking plumes which merged together so that their spacing increased progressively with depth. They inferred that there would be a self-similar convective structure with a continuously varying scale. On the other hand, numerical experiments by Cattaneo *et al.* (1991) showed a large-scale pattern with long-lived sinking plumes, together with weaker, irregular motions, producing ephemeral plumes that were swept into nodes of the large-scale network and therefore disappeared. If the large-scale structures are interpreted as supergranules then these disorganized motions would correspond to mesogranules. Thus behaviour found in numerical studies of convection in stratified layers is strongly model-dependent.

As we have already emphasized, observations and kinematic models of surface motions support an alternative picture, with discrete scales of convection. We have argued that granules and supergranules are distinct phenomena (though both must be accompanied by inertial subranges leading to motions on scales where energy can be dissipated). Such a hierarchy would be expected if there are nested unstable boundary layers and may be related to the successive ionization of H and He (Simon & Leighton 1964; Gierasch 1985). But how many such scales exist in the convective zone? The shallow radiative boundary layer at the photosphere may well be liable to shear instabilities but any temperature fluctuations would be ironed out. At greater depths there should be structures which extend throughout the full depth of the convective zone. So the presence of granules and supergranules suggests that there should also be giant cells with diameters of 200–400 Mm (Simon & Weiss 1968). This is a simple and attractive argument but, despite persistent attempts to detect them over the last 25 yr, these giant cells have never been observed. Although they may be screened from sight (Stix 1981; van Ballegoijen 1986), it is time to question their existence.

At the base of the convective zone the radiative and adiabatic gradients are equal. The bulk of the layer above is adiabatically stratified and the radiative conductivity decreases upwards, so energy transport by radiation falls off with increasing radius. Fig. 1 shows the variation with depth,  $z$ , below the photosphere, of the fraction,  $f$ , of the total energy flux that is carried by radiation, derived from Spruit's (1977) model of the convective zone. At its base ( $z = 200$  Mm)  $f = 1$  but the value of  $f$  drops to 0.07 at  $z = 100$  Mm. In the lower region the curve can be approximated by an exponential of the form  $f = \exp[(z - z_0)/Z]$  with a scaleheight  $Z = 40$  Mm. This reduction in the radiative flux acts as a heat source distributed over the lower part of the convective zone, such that half the total energy flux is deposited in the bottom 30 Mm. Convection has to cool this region and carry

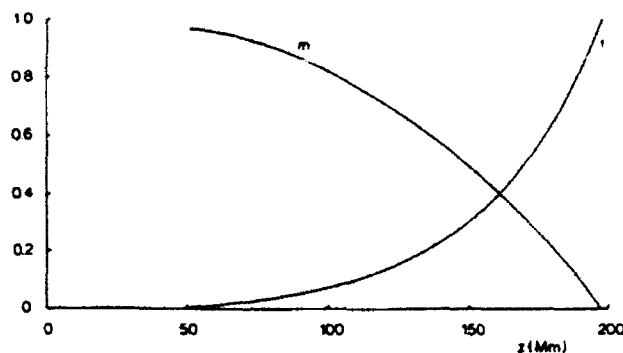


Figure 1. Radiative heating in the lower part of the convective zone. The fraction  $f$  of the total energy flux that is carried by radiation (equal to the ratio of the radiative to the adiabatic gradient) as a function of depth  $z$  below the photosphere. Also shown is the fraction  $m$  of the total mass of the convective zone that lies below the depth  $z$ . [From Spruit's (1977) model of the solar convection zone.]

energy outward until it can be radiated from the photosphere but, owing to conservation of mass, this cannot be achieved simply by bringing material from the base of the zone up to the photosphere. Fig. 1 also shows the fraction,  $m(z)$ , of the mass of the convective zone that lies below a depth  $z$ : because of the density stratification, half the mass lies within 50 Mm of the base and 93 per cent is in the lower half of the convective zone.

There is an instructive analogy with Boussinesq convection driven by internal heating. Numerical experiments on a fluid with infinite Prandtl number (motivated by convection in the Earth's mantle) show an upper thermal boundary layer from which narrow cold plumes descend to cool the region below (McKenzie, Roberts & Weiss 1974; Lennie *et al.* 1988). As the rate of heating is increased the boundary layer becomes unstable and the spacing between the sinking plumes diminishes. In both two- and three-dimensional models the horizontal scale is therefore smaller than the layer depth.

These calculations suggest that supergranules may actually represent the dominant scale throughout the whole convective zone, as has been proposed by Zahn (1987; see also Rieutord & Zahn 1991). In this picture there is a layer near the base of the convective zone, which is heated by radiation and cooled by slender plumes descending rapidly from just below the surface (compensated by a weak general upward motion). These plumes emerge from supergranules, whose horizontal scale is determined by local processes, within, say, 10 Mm of the photosphere. As they fall, adjacent plumes may merge so as to allow a modest increase in their spacing with increasing depth. At the base of the convective zone the horizontal scale is then comparable with the thickness of the layer ( $\sim 40$  Mm) where energy is deposited by radiation (Spiegel 1968).

In a stratified layer this process is possible only if a sinking plume entrains material sufficiently rapidly to maintain its cross-sectional area. To model such behaviour we consider an adiabatically stratified plane layer. In a steady state the rate of turbulent entrainment is found empirically to be proportional to the velocity  $w$  of the sinking plume, so that the inflow velocity  $u = \alpha w$  with  $\alpha \approx 0.1$  (Turner 1973, 1986; Schmitt, Rosner & Bohn 1984). Conservation of mass then

requires that the rate of change of the radius  $b$  is given by

$$\frac{db}{dz} = \alpha - \frac{1}{2} b \left( \frac{1}{H_\rho} - \frac{1}{H_u} \right), \quad (1)$$

where  $H_\rho$  is the density scaleheight and the velocity scaleheight  $H_u = -(d \ln w / dz)^{-1}$ . We expect the velocity to decrease slowly with increasing depth, so the radius increases downwards if  $b/H_\rho < 2\alpha \approx 0.2$ . In the middle of the layer, where  $H_\rho \approx 60$  Mm, a plume with radius less than 12 Mm will continue to expand. If we assume that  $H_u \gg H_\rho = \frac{1}{2} z$  then (1) can be integrated to give

$$b = (b_0 - \frac{1}{2} \alpha z_0)(z_0/z)^{1/2} + \frac{1}{2} \alpha z, \quad (2)$$

so that a plume with a radius  $b_0 = 1$  Mm at a depth  $z_0 = 10$  Mm would expand to a radius of 8.6 Mm at 150 Mm depth. (For  $z$  sufficiently large, the right-hand side of (2) is dominated by the final term.) Thus we suggest that the layer at the base of the convective zone may be cooled by narrow sinking plumes with diameters of 10–20 Mm, separated by distances of 30–40 Mm. This picture needs to be confirmed by detailed investigations which include the full dynamics of convection. Preliminary results from two-dimensional numerical experiments are inconclusive.

#### 4 DISCUSSION

In the past three decades there have been tremendous advances in our understanding of non-linear convective processes, obtained through increasingly sophisticated numerical modelling. At the same time, observers have tried, using various diagnostics and tracers, to determine scale sizes in the convective zone. Granules and supergranules are distinct phenomena with very different scales, while meso-granules are less clearly defined. We interpret them as secondary products of the supergranules, and propose that they are coupled to granular convection so as to produce exploders. The concept of giant cells no longer seems appropriate for the Sun. Guided by observations, we propose instead that supergranules generate rapidly sinking plumes that penetrate to the base of the convective zone, so that there is no need to postulate convective structures with larger horizontal scales. This qualitative picture needs to be confirmed by further detailed computations. Current three-dimensional calculations are impressive but the results remain inconclusive except for motion near the surface. Since it is difficult to model turbulent entrainment in numerical experiments, it may be preferable to study the dynamics of isolated plumes (Schmitt *et al.* 1984). Theory will be increasingly constrained as more detailed observations, including spectroscopic measurements of velocities and magnetic fields, become available. Behaviour in the Sun must also be reconciled with that in other stars, notably red giants, where large-scale structures are observed (Buscher *et al.* 1990).

Sinking plumes are deflected by Coriolis forces or any large-scale circulations. Moreover, an array of closely spaced plumes itself affects the transport of angular momentum and the distribution of magnetic fields in the convective zone. The effect on differential rotation can be modelled by introducing an anisotropic viscosity (Rüdiger 1989) which eliminates radial shear but allows a latitudinal variation in

angular velocity (*cf.* Rieutord & Zahn 1991). Such a model might lead to a rotation pattern like that inferred from solar oscillations (Dziembowski *et al.* 1989). A similar process would pump magnetic flux downwards and help to retain magnetic fields in the convective zone. Understanding the structure of convection therefore opens the way to producing a realistic model of the solar dynamo.

#### ACKNOWLEDGMENTS

We thank Fausto Cattaneo, Greg Ginet, Neal Hurlburt, Andrea Malagoli, Larry November, Robert Rosner, Edward Spiegel, Alan Title, Juri Toomre, Jean-Paul Zahn and Jack Zirker for helpful comments and suggestions. We are also grateful for support from the UK Science and Engineering Research Council and the Window-on-Science Program of the US Air Force Office of Scientific Research.

#### REFERENCES

- Bergé, P. & Dubois, M., 1979. *J. Phys. Lett.*, **40**, L505.  
 Bray, R. J., Loughhead, R. E. & Durrant, C. J., 1984. *The Solar Granulation*, 2nd edn. Cambridge University Press, Cambridge.  
 Buscher, D. F., Haniff, C. A., Baldwin, J. E. & Warner, P. J., 1990. *Mon. Not. R. astr. Soc.*, **245**, 7p.  
 Busse, F. H., 1981. In: *Hydrodynamic Instabilities and the Transition to Turbulence*, p. 97, eds Swinney, H. L. & Gollub, J. P. Springer, Berlin.  
 Cattaneo, F., Brummell, N. H., Toomre, J., Malagoli, A. & Hurlburt, N. E., 1991. *Astrophys. J.*, **370**, 282.  
 Dziembowski, W., Goode, P. R. & Libbrecht, K. G., 1989. *Astrophys. J. Lett.*, **337**, L53.  
 Gierasch, P., 1985. *Astrophys. J.*, **288**, 795.  
 Hurlburt, N. E., Toomre, J. & Massaguer, J. M., 1984. *Astrophys. J.*, **282**, 557.  
 Jones, C. A. & Moore, D. R., 1979. *Geophys. Astrophys. Fluid Dyn.*, **11**, 245.  
 Lennie, J. B., McKenzie, D. P., Moore, D. R. & Weiss, N. O., 1988. *J. Fluid Mech.*, **188**, 47.  
 McKenzie, D. P., Roberts, J. M. & Weiss, N. O., 1974. *J. Fluid Mech.*, **62**, 465.  
 Massaguer, J. M., 1990. In: *Inside the Sun*, p. 101, eds Berthomieu, G. & Cribier, M., Kluwer, Dordrecht.  
 Muller, R., Roudier, T., Vigneau, J., Frank, Z., Shine, R. A., Tarbell, T. D., Title, A. M. & Simon, G. W., 1990. *Publ. Debrecen Obs.*, **7**, 44.  
 Muller, R., Roudier, T., Vigneau, J., Frank, Z., Shine, R. A., Tarbell, T. D., Title, A. M., Topka, K. P. & Simon, G. W., 1991. *Nature*, submitted.  
 November, L., 1989. *Astrophys. J.*, **344**, 494.  
 November, L., Toomre, J., Gebbie, K. & Simon, G. W., 1981. *Astrophys. J. Lett.*, **245**, L123.  
 Rieutord, M. & Zahn, J.-P., 1991. In: *The Sun and Cool Stars. Activity, Magnetism, Dynamics*, p. 33, eds Tuomunen, J., Moss, D. & Rüdiger, G., Springer, Berlin.  
 Rüdiger, G., 1989. *Differential Rotation and Stellar Convection: Sun and Solar-type Stars*, Gordon & Breach, New York.  
 Schmitt, J. H. M. M., Rosner, R. & Bohn, H. U., 1984. *Astrophys. J.*, **282**, 316.  
 Simon, G. W. & Leighton, R. B., 1964. *Astrophys. J.*, **140**, 1120.  
 Simon, G. W. & Weiss, N. O., 1968. *Z. Astrophys.*, **69**, 435.  
 Simon, G. W. & Weiss, N. O., 1990. *Astrophys. J.*, **345**, 1060.  
 Simon, G. W., Title, A. M. & Weiss, N. O., 1991. *Astrophys. J.*, **375**, 775.  
 Simon, G. W. *et al.*, 1988. *Astrophys. J.*, **327**, 964.